Domínguez-Santos *et al.*
Int J Concr Struct Mater (2025) 19:52
https://doi.org/10.1186/s40069-025-00793-1

International Journal of Concrete Structures and Materials

RESEARCH Open Access

Reinforced Concrete with Graphene Oxide: Techno-Economic Feasibility for Reduced Cement Usage and CO_2 Emissions

D. Domínguez-Santos[1], P. Muñoz[2,3*], J. O. Morales-Ferreiro[4], C. Acuña[5], D. E. Diaz-Droguett[5,6] and Elvira Villaro[7]

Abstract

Concrete, a key material in modern infrastructure, significantly contributes to global CO_2 emissions, urging innovative approaches for its environmental impact mitigation. This study evaluates the techno-economic feasibility of incorporating graphene oxide (GO) into concrete formulations to enhance mechanical properties and reduce cement usage, thereby mitigating CO_2 emissions. The methodology involved synthesising GO using a modified Hummers' method, ensuring uniform dispersion in concrete matrices. Concrete samples with varying GO contents underwent mechanical strength testing, as well as microstructural analysis including SEM, XPS, and Raman spectroscopy. Results led to simulations of the mechanical response of low- and medium-rise buildings subjected to seismic forces. Besides, economic assessments were performed by considering the overall cost of materials (GO and concrete) and the savings from CO_2 emissions, based on different scenarios for both GO and CO_2 prices. The optimal formulation uses 0.1% GO by weight of cement, improving compressive strength by up to 17.92% and flexural strength by up to 74.78%. Structural models indicate that GO can reduce the weight of structural elements by 8–24%, leading to lower seismic forces and easier compliance with seismic-resistant standards. Economic analysis reveals that low-rise buildings can benefit from GO-enhanced concrete if the GO price is between €50 and €80 per kg, depending on CO_2 credit prices ranging from €60 to €200 per tonne. For taller buildings, the economic feasibility is more restrictive; GO prices must be between €50 and €70 per kg with CO_2 credit prices starting at €100 per tonne to justify the use of 0.1% GO.

Keywords Mechanical response, Graphene oxide, Concrete, Economy, CO_2

Journal information: ISSN 1976-0485 / eISSN 2234-1315.

*Correspondence:
P. Muñoz
pedro.munoz@unir.net
Full list of author information is available at the end of the article

Graphical Abstract

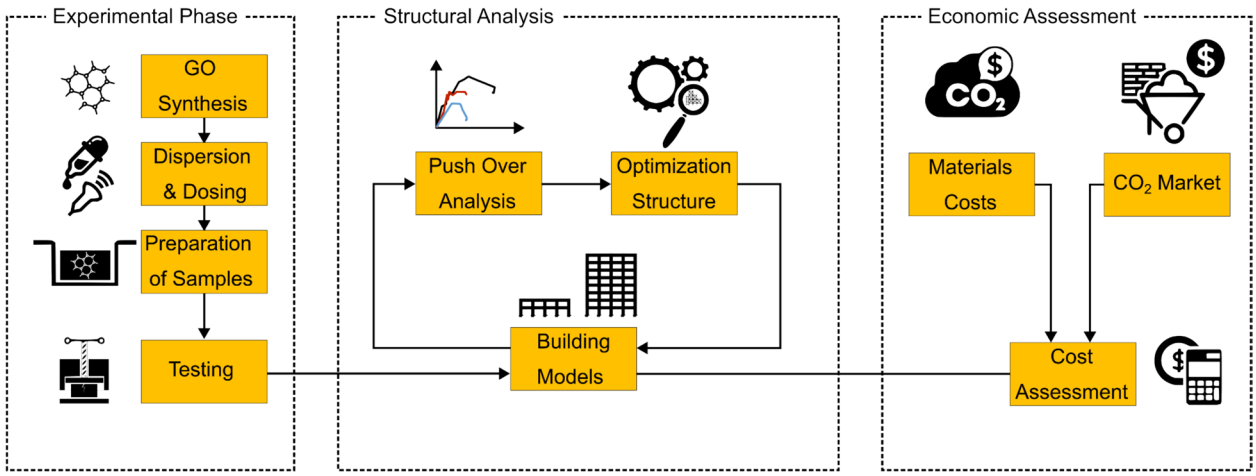

1 Introduction

Concrete has been instrumental in shaping modern society, providing strength, adaptability in shaping, and economical production for the construction of safe and reliable infrastructure. However, traditional concrete manufacturing processes have become increasingly scrutinised in recent decades due to their significant environmental impact, accounting for approximately 8% of the world's carbon dioxide emissions (International Energy Agency, 2022). In this respect, reducing the carbon footprint of the construction industry has emerged as a global priority. For instance, Europe aims to reduce CO_2 emissions from the concrete industry by 59 kg per tonne of produced concrete by 2050. This concern necessitates a framework that encourages new investments in the concrete industry to achieve sustainable goals (Bacatelo et al., 2023).

The primary environmental impact of concrete production stems from its energy-intensive process, which involves high temperatures of around 1500 °C to produce cement. For every kilogram of cement produced, nearly one kilogram of CO_2 is emitted as a by-product (Galusnyak et al., 2022). Various strategies have been explored to mitigate this impact, including the use of alternative binders, carbon capture techniques, and the replacement of traditional cement with recycled materials or nanotechnology (Tayebani et al., 2023).

Replacing natural raw materials with residues and/or by-products has certainly shown promise in reducing resource depletion and lowering the CO_2 footprint of concrete. Some of these materials have successfully resulted in lighter concretes with lower thermal conductivity due to a higher porosity (Haddadian et al., 2023), others, such as fly ash, blast furnace slag, and glass powders, act as supplementary cementing materials, enhancing mechanical properties by increasing the amount of CSH/CaSH or Si phase (Chung et al., 2020).

Recycled aggregates, typically exhibit higher porosity and water absorption than natural aggregates, which can lead to increased permeability, reduced durability, and lower mechanical strength in the resulting concrete (Onaizi et al., 2021). Thus, additional measures, such as advanced processing techniques or optimised mix designs, may be required to achieve performance levels comparable to conventional concrete, potentially offsetting the initial environmental and economic benefits.

Cement replacement materials, like fly ash and blast furnace slag, among others, certainly can enhance mechanical properties to some extent by improving its density and reducing permeability. However, their performance is highly variable and dependent on the specific mix design which hinders standardization (Alex et al., 2022). Besides, some supplementary cementitious materials such as fly ash and slag may pose risks related to leaching and toxicity since it can contain trace amounts of heavy metals (e.g., arsenic, chromium, or mercury) or other potentially harmful substances inherited from their industrial origins (Krishnan et al., 2024).

In addition to the aforementioned solutions, nanomaterials, such as nano-silica and carbon nanotubes, have also emerged as an efficient means of improving concrete's mechanical properties and durability by reducing the necessary amount of traditional cement while maintaining similar strength, ultimately leading to a reduction

in the size of the required structural elements (Labaran, 2024). However, they often come with challenges related to uniform dispersion, production issues for large quantities and potential health hazards (Sanalkumar & Yang., 2024).

In contrast, GO offers a unique combination of a large specific surface area, ease of production in large quantities, and reduced health and environmental risks (Iqra & M., 2024). Therefore, the selection of graphene oxide (GO) as an additive in concrete is driven by its superior mechanical properties compared to other alternatives aimed at reducing the carbon footprint of concrete, such as recycled aggregates, cement replacement materials, and other nanomaterials. Studies have pointed out that the small doses of GO (commonly ranging from 0.01 to 0.3 wt.%) can significantly enhance the mechanical behaviour and fire performance of concretes (Rao et al., 2024). Additionally, GO's ability to improve the durability of concrete under extreme environmental conditions further underscores its potential (Udumulla et al., 2024). Moreover, GO-enhanced concrete has been found to reduce greenhouse gas emissions (Tarpani et al., 2024).

Due to these exceptional properties, graphene oxide (GO) has garnered significant attention over the past two decades as a potential key factor for reducing the building sector's carbon footprint. It is projected to gain increasing importance in the construction industry (Zhang et al., 2024).

Although numerous studies have investigated the effects of graphene, most have focused on enhancing cement paste or mortars, with fewer dedicated exclusively to concrete (Shamsaei et al., 2018). These studies have demonstrated that for cementitious materials the optimal content of GO (ranging between 0.03% and 0.06% by weight) leads to remarkable improvements, such as a 77.7% increase in compressive strength and a 37.5% increase in tensile strength. Flexural strength also improves, with gains up to 70%. These enhancements are attributed to the refinement of the pore structure, with a reduction in average pore diameter by 36.7% and a decrease in total porosity by 25.5%. GO's ability to serve as a nucleation site for hydration products results in a denser and more uniform microstructure, thus contributing to the improved mechanical performance (Liu et al., 2021).

Besides, studies have further underscored the advantages of GO in terms of water sorptivity and chloride penetration. Although the effectiveness strongly depends on GO fraction, its addition to cement matrix can effectively enhance its resistance to aggressive elements by forming a strong barrier that can reduce the movement of aggressive chemicals. Additionally, GO reacts with calcium hydroxide ($Ca(OH)_2$) during cement hydration, facilitating the formation of additional calcium silicate hydrate (C-S-H) gel. This reaction refines the pore structure, thereby reducing capillary action and water ingress, and further limiting the conditions necessary for corrosion. For instance, concentrations of GO between 0.02% and 0.1% by weight of cement may achieve reductions of up to 50% in chloride ion penetration and water permeability coefficients, compared to standard concrete (Luo et al., 2022). These effects certainly enhance the concrete durability and increase the life-span of concrete based structures (Luo et al., 2022; Mohammed et al., 2015). Additionally, the environmental impacts of GO production have been also analysed, suggesting methods to reduce its carbon footprint (Onaizi et al., 2021; Zhang et al., 2024).

However, these benefits of GO may not be fully achieved unless it is uniformly dispersed in the matrix. Achieving uniform GO dispersion in concrete mixtures is crucial for extending GO's application in the concrete industry (Green & Hersam, 2010), as its chemical inertness and hydrophobic nature may lead to entangled clumps, reducing the mechanical strength by promoting local stress concentrations (Divya et al., 2023). The time dispersion effect, as demonstrated by Divya et al. (Murali et al., 2022), is notable. For instance, these authors found that with an equal GO dosage, compressive strength improved by 40% and flexural strength by 70%, when the time dispersion increased from 30 to 60 min (Walunjkar & Bajad, 2023). This tendency to agglutinate limits the maximum amount of GO that can be added to approximately 0.1% by weight (wt.%) (Liu et al., 2021; Monteiro et al., 2017). For instance, in M20 grade concrete, the maximum increase in strength is found at a GO dosage of 0.03 wt.% (Monteiro et al., 2017); however, above 1.0 wt.%, the strength tends to decrease (Liu et al., 2021).

In addition to the procedures required for uniform GO dispersion in concrete mixtures, the production scalability of GO concrete is mainly limited by the cost of GO. As stated by Haddadian et al. (Haddadian et al., 2023), further research is needed to persuade construction professionals that GO is a viable option for the enhancement of concrete. These authors highlighted that the cost-effectiveness of materials strengthened by GO remains a major barrier to its widespread application in the construction industry With GO prices ranging from 100 to 250 €/kg—making it 5 to 10 times more expensive than conventional cement (Tallentire, 2022)—ensuring the economic viability of GO concrete requires substantial reductions in structural dimensions. These reductions are made possible by the improved mechanical performance

of GO-enhanced concrete. For instance, one notable example indicates, for a pilot building, using all conventional equipment and labour, a 30% less material for comparable performance to a standard RC30 concrete and removed all steel reinforcement, further reducing associated costs and emissions, but no clear economic benchmarks were reported (Ikram et al., 2020). Moreover, some studies have suggested that the long-term benefits of GO-enhanced concrete, such as increased resistance to the penetration of chloride and sulfate ions (Udumulla et al., 2024), could result in additional savings during the operational phase through reduced maintenance and extended service life (Labaran, 2024; Tarpani et al., 2024). Furthermore, a reduced volume of cement or maintenance results in a smaller carbon footprint for buildings. Studies indicate that enhancing concrete performance by 25% through the incorporation of graphene could lead to a 2% reduction in CO2 emissions throughout the supply chain (Ikram et al., 2020). This decrease in CO2 emissions could, in the current emissions market or in the near future, represent an additional improvement that would enhance the economic balance due to the reduced need for cement in GO-enhanced concrete structures. However, to the best of our knowledge, the literature does not contain techno-economic assessments that address the incorporation of GO in concrete from a global perspective applied to building construction.

Therefore, by considering these concerns, this paper aims to provide a balanced perspective by highlighting both the mechanical and economic benefits of GO, as well as the environmental considerations. By addressing these gaps, this research contributes to a more comprehensive understanding of GO-enhanced concrete, paving the way for its broader adoption in the construction industry. First, the processes for GO production and sample manufacturing are described, followed by mechanical testing to simulate building models using push-over analysis (i.e., a simplified nonlinear technique to estimate seismic structural deformations). This study evaluates the overall cost of two types of buildings: a two-storey and eight-storey structure, by considering concrete and GO acquisition costs, as well as the price of carbon credits attributed to reduced concrete usage, thereby leading to lower CO_2 emissions. The objective is to encourage the construction industry to proactively consider the use of GO concrete in sustainable development.

2 Materials and Methods

2.1 Synthesis of GO

GO solution was prepared using a variation of the modified Hummers' method (Indukuri et al., 2019; Nanjundappa et al., 2023). The procedure consisted of mixing 1 g of graphite flakes, 0.5 g of $NaNO_3$, and 25 ml of H_2SO_4 under magnetic stirring. Then, 3 g of $KMnO_4$ was added. To complete graphite oxidation, the new mixture was stirred for 3 h. Afterwards, 10 ml of H_2O_2 aqueous solution at 3% was incorporated, turning the solution slightly yellowish. The obtained graphite oxide was washed with a 10 ml solution of HCl. The pH was adjusted by the addition of an aqueous solution of NaOH. The exfoliation process of the graphite oxide was carried out by sonication using an ultrasonic bath (40 kHz). Following this, centrifugation cycles at 4100 rpm were performed to collect the supernatant and obtain the GO solution. The resulting GO was diluted with distilled water and then ultrasonicated for 30 min, to produce the stable aqueous GO solution. This process corresponded with the steps described by Indukuri et al. (Yang et al., 2017). However, although the inclusion of GO in concrete products certainly leads to improvements in mechanical strength (Meddage et al., 2024), the low dispersal propensity of GO may cause agglomeration in the cement matrix due to the negatively charged GO and the high concentration of alkaline ions (e.g. Ca^{2+}, Na^{+}, and K^{+}) (Fonseka et al., 2024). Besides, the dispersion technique and time are critical for ensuring the reproducibility of GO synthesis and its performance in concrete. GO tends to agglomerate due to Van der Waals forces and hydrophobic tendencies, creating clusters that hinder its uniform distribution in the cement matrix. This study employed ultrasonic mixing, which is recognised as being the most effective dispersion method for achieving nanoscale exfoliation and uniformity in GO solutions. High-frequency sound waves break down GO agglomerates, producing optimal dispersion and enhancing the mechanical properties of GO-added concrete (Fonseka et al., 2024). To overcome the challenges posed by GO's high surface energy and hydrophilic–hydrophobic nature (e.g. spalling and the development of stress concentrations), resultant GO solutions were further diluted with tap water. The solution was mixed with deionised water and mechanically stirred for 3 h at 1000 rpm, then it was sonicated for 3 h with a soaking time of 18 h. Finally, the mixture was stirred while undergoing sonication again for 1 h before mixing with cement and aggregates.

Therefore, the followed method aligns with the need for extended sonication times, to ensure uniform dispersion and prevent defects within the matrix. This approach is consistent with the findings in the literature (Dhemla et al., 2022; Murali et al., 2022; Qureshi & Panesar, 2020) and the GO solution produced remained stable for several weeks without visible precipitation (Fig. 1).

2.2 GO Characterisation

A field-emission scanning electron microscope (FESEM) (JEOL JSM-6610LV) was used to characterise the

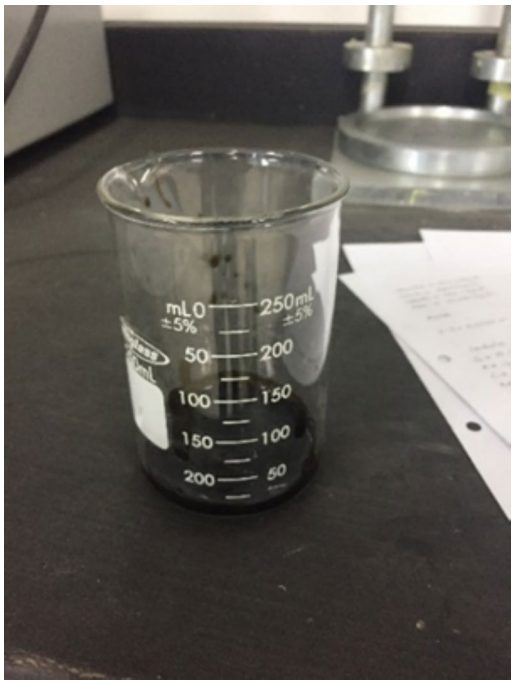

Fig. 1 GO solution

morphology and surface composition of the GO materials. The X-ray photoelectron spectroscopic (XPS) study was performed using a Kratos Axis 165 spectrometer. A monochromatic AlKα (1486.6 eV) radiation source, with an energy resolution of 0.4 eV at a pass energy of 20 eV, was used at a current of 15 mA and a voltage of 15 kV. To quantify the defect density of the synthesised samples, a micro-Raman analysis was performed using a 514.5 nm laser excitation (2.41 eV) using a Bruker SENTERRA dispersive Raman microscope. Agilent and Witec Alpha 300S atomic force microscopes (AFMs) were employed to analyse and measure the thickness of the graphene flakes.

2.3 Sample Preparation

A total of four mixes, including conventional concrete (i.e., 30 MPa), were prepared. For each series, nine specimens were manufactured. The varying percentages of GO were determined by the Taguchí methodology (Balaji & Swathika, 2022), based on the common ranges typically found in the literature (i.e., approximately 0.01–0.10 wt.% or about 0.3–3.0 kg per cubic metre of concrete) (Hong et al., 2022; Lin & Du, 2020; Wang et al., 2017). Thus, the GO concentrations selected for this study were set at 0.05%, 0.10%, and 0.20% by weight of cement. Previous research has shown that GO dosages below 0.2% optimize mechanical properties, including compressive, flexural, and tensile strengths, while avoiding the agglomeration issues observed at higher concentrations (Zeng et al., 2022). Specifically, Zeng et al. (2023) (Qin et al., 2017) and Liu et al. (2017) (Liu et al., 2021) reported that concentrations in the range of 0.03–0.10% significantly enhance hydration, refine pore structure, and improve crack resistance, with 0.1 wt% being particularly effective for ordinary concrete. These improvements are attributed to GO's high specific surface area and nucleation properties, which promote cement hydration and strengthen interfacial bonding. Experimental evidence further indicates that, at concentrations exceeding 0.2%, the risk of agglomeration increases, potentially undermining mechanical performance (Fonseka et al., 2024; Kurda et al., 2022). Thus, the selected concentrations represent an optimal range, balancing performance enhancements, material costs, and practical dispersion considerations.

Moreover, the distribution of aggregates was determined by the Faury-Joisel method (Asem et al., 2021), which determines the proportion of aggregates based on an ideal curve. To determine the mass distribution of the aggregates, the stockpile was sampled in accordance with ISO 20290–1:2021. From the collected data, the ideal granulometric curve obtained with the Faury-Joisel method was achieved (Fig. 2). As a result, the combined percentage of sand and cement was set at 52 wt.%. A standard type of cement was used, with a water-to-cement ratio of 0.43. Samples were mixed using an automatic mixer. The loading sequence was as follows: 70% of the total mixing water was introduced and then 8% coarse aggregates, fine elements and cement were sequentially loaded; finally, the remaining amount of water (25 wt.%) was added and the mixer run for approximately 2 min until a homogeneous blend was achieved.

Curve L represents the ideal grain size band. Line Y represents the intersection of the gravel and sand curves, while line X represents the intersection of curve L and curve Y.

For casting, the Abrams cone settlement method was followed, in accordance with ISO 1920–2:2016, to determine the appropriate workability. The test yielded a settlement of 1 cm, complying with the requirements established by the standard (Fig. 3).

Finally, the concrete was cast into cylindrical (ø 300×150 mm) and prismatic (530×150×150 mm) moulds, while air was removed by vibrating. The demoulding of the samples occurred after 20 h. Subsequently, the samples were cured in water saturated with lime at a temperature of 23 ± 2 °C and a relative humidity of 90% for 7, 14, and 28 d. All the specimens tested were meticulously prepared, taking into account the water absorption of aggregates, to accurately determine the required amount of materials for the mixture (Table 1).

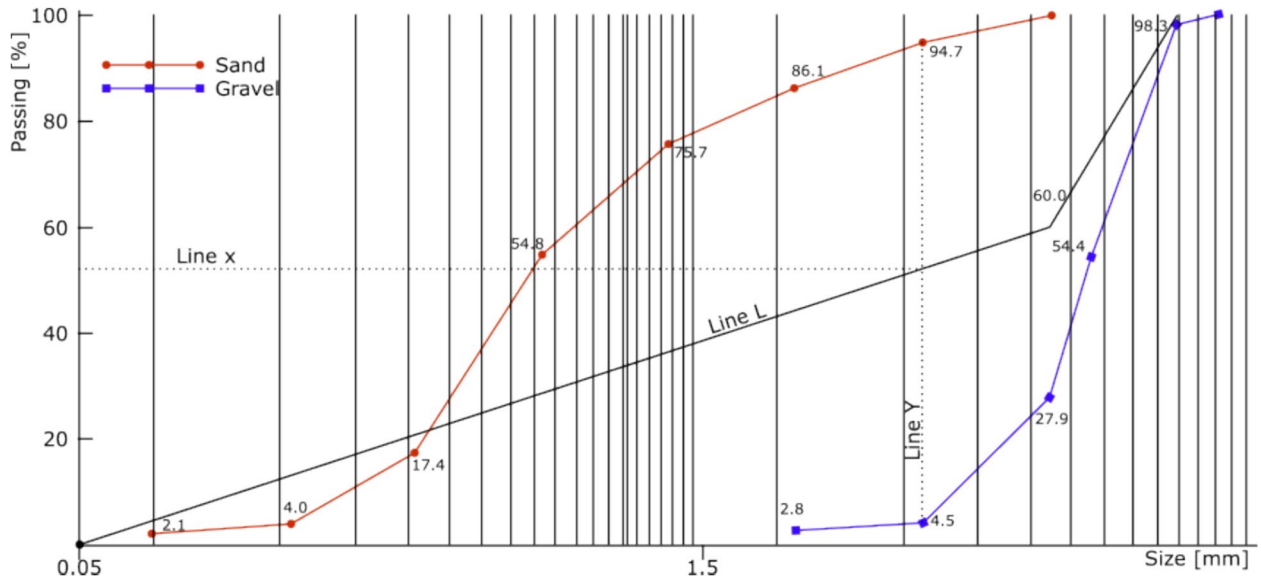

Fig. 2 Particle size distribution in accordance with the Faury-Joisel curve

Fig. 3 Abrams cone test for determining the workability of concrete samples

2.4 Testing

Compression tests were carried out on cylindrical specimens at 7, 14, and 28 d, using a universal testing machine. Before testing, a 3 mm plastic sulphur mortar layer was applied to the surface with the aim of removing any imperfections (Fig. 4a). The contact of the specimen with the machine was made through a 10 mm-thick cylindrical metal plate and a constant load speed of 1 kN/s was applied until collapse. The flexural strength was measured in prismatic test pieces at 28 d, following ISO 1920–4:2020 (Fig. 4b). The flexural test was conducted using a 'Tecnotest P 433/C' hydraulic press, following

Table 1 Mix proportions expressed in kg per cubic metre of concrete

ID	Gravel	Sand	Cement	Water	GO	GO**
G30	1035	706	411	172 (204)*	–	–
G30a	1035	706	410.3	172 (204)*	0.20	0.05%
G30b	1035	706	410.3	172 (204)*	0.41	0.10%
G30c	1035	706	410.3	172 (204)*	0.82	0.20%

*The values in parentheses correspond to the amount of water, considering aggregate absorption

**The values express the percentage relative to the cement content

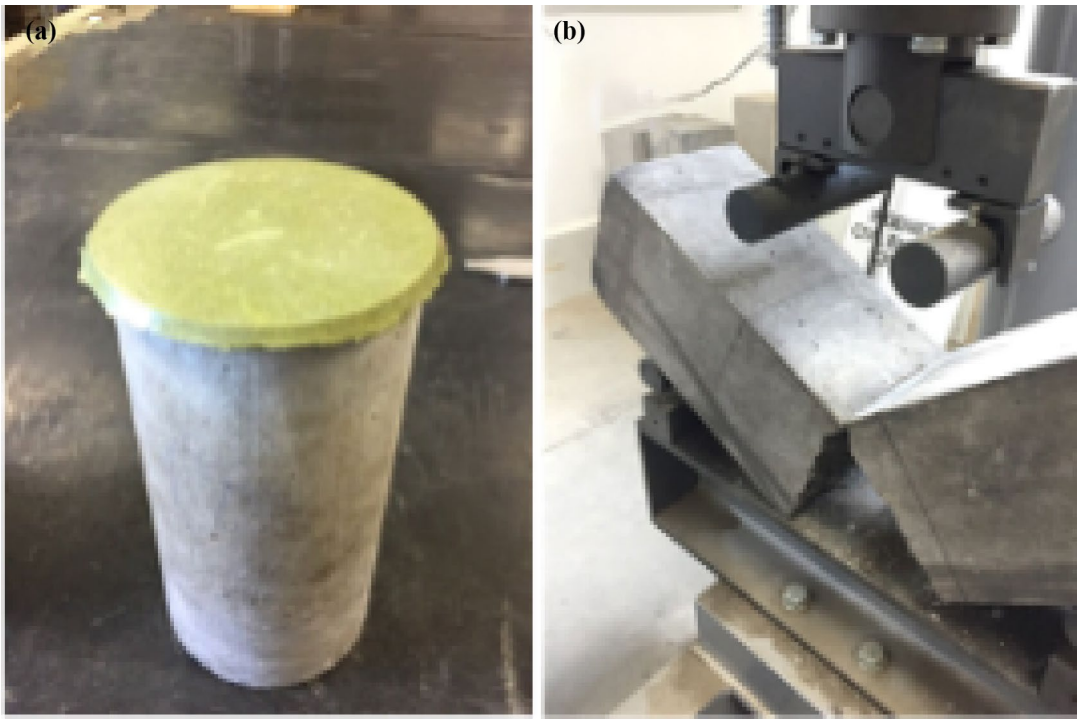

Fig. 4 Photography of **a**) cylindrical samples for compression testing and **b**) flexural strength testing in prismatic samples

the specifications of standard NCh 1038. This document specifies the placement of the applied load on the specimen within the central third of its span (i.e., loads were gradually applied at 7.5 cm from the central point). In characterising the tested specimen:

$$L \geq 3h \tag{1}$$

where: L is the span length, h is the specimen height.

Once the specimen was prepared, the testing began. The load application rate, per the standard, must not exceed 0.016 N/mm^2/s (Yang et al., 2017) or 1.6 N/cm^2/s, which aligns with the unit used by the machine. For this test, a constant load of 1 N/cm^2/s was applied. Upon reaching the failure limit, the data obtained were recorded.

The load application points on the hydraulic press were symmetrically positioned relative to the midpoint of the specimen, as shown in the attached image.

Depending on the fracture location, the flexural tensile strength was calculated using the following equations, by distinguishing whether the fracture occurred within the central third of the span (Eq. 2) or outside the central third of the span (Eq. 3) (Małkowski et al., 2018):

$$R = \frac{P \cdot L}{b \cdot h^2} \tag{2}$$

$$R = \frac{3 \cdot P \cdot a}{b \cdot h^2} \tag{3}$$

where: where P is the maximum applied load (N), L is the span length (mm), b is the average width of the specimen at the fracture section (mm), h is the average height of the specimen at the fracture section (mm), and a is the distance between the fracture section and the nearest support, measured along the midline of the lower surface of the specimen (mm).

The modulus of elasticity (E) was measured in cylindrical samples during the compression strength tests via a combined compress meter and extensometer, which provided numerical values and stress–strain curves. Thus, the average Young's modulus (E_a) can be calculated (Eq. 4) as the slope of the straight line in the stress–strain curve, i.e., between the end of the compaction phase (X_1,Y_1) to the beginning of the stable fracturing phase (X_2,Y_2) (Fraser, 2000).

$$E_a = \frac{(Y_2 - Y_1)}{(X_2 - X_1)} \tag{4}$$

In addition, ductility was calculated during these tests, as this dimensionless parameter is determined by the relationship between the ultimate strain (ε_u) and the yielding strain (ε_y), as determined from the capacity curves of the samples. The final deformation of each sample was determined through the last point of the capacity curve before the decrease in its resistance, while the plastic deformation was obtained using the procedure established by FEMA Standards P1050 and ATC-40.

2.5 Building Modelling and Calculations

The choice of the framework structure in the analyses in this research was made to the abundance of this construction system in many countries with low, medium, and moderate seismicity in Latin America and Europe (Dominguez et al., 2017). These structures are characterized by their rapid construction times and minimal resource requirements. The small sections of the structural elements that make up this type of structure make it relatively inexpensive compared to shear wall systems. On the other hand, the low lateral stiffness of these constructions is compensated for by brick walls (non-structural infill walls) used in enclosures and partitions (Domínguez et al., 2016).

For this research, two-storey and eight-storey buildings were used, where each storey was 3 m high, corresponding to building heights of 6 and 24 m, respectively. Each building also contained 4 bays, each measuring 5 m in height. The building models had a regular elevation, following the design recommendations established by most seismic-resistance standards. The use of this structural model was a consequence of its reliability, in relation to the results obtained for the required computational analysis. The effectiveness of these methods has been shown in other research (European Committee for Standardization, 1992).

For the design of the structural sections (columns and beams), the requirements established by the European Standard EC-2 (Fomento, 2008) and the Spanish Standard EHE-08 (European Committee for Standardization, 1998) for reinforced concrete were followed. Additionally, the design criteria established by the European seismic Standard EC-8 (Fomento, 2002) and the Spanish standard NCSE-02 (Scott & Fenves, 2006) were followed to determine the horizontal loads. The seismic zoning linked to this structural typology necessitated the use of these standards (European Committee for Standardization, 1992).

The materials used for the structural elements (beams and columns) were HA-30 concrete, which has a characteristic strength of f_{ck} = 300 kg/cm^2, and high-strength B-500-S steel, which has a yield strength of f_{yk} = 5,000 kg/cm^2. The effect of GO on the analyses was assessed by incorporating the material properties obtained from laboratory tests. Thus, the GO-enhanced concrete was been considered as a unique element with the measured properties: Compressive Strength (kPa), Tensile Strength (kPa), Modulus of Elasticity (kPa), Strain at Peak Stress (m/m) and Density (kN/m^3).

The loads considered in the structural calculations followed the combination of actions G + 0.3Q from Eurocode 8 (Fomento, 2002). In the combination of actions, 'G' represents the weight of the structure, while 'Q' represents the live loads corresponding to residential, administrative, or small business use, and is equivalent to 2 kN/m^2. This load was applied to all floors of the frame except for the top floor (roof), where the load was 1 kN/m^2 (maintenance use only).

Finally, on all floors of the portal frames, a rigid diaphragm (infinitely rigid element) corresponding to a 30 cm floor slab was considered as an element limiting possible displacements in the vertical axis. The dimensions of the sections used in the models are detailed in Fig. 5. Based on this preliminary design and by varying the properties of each type of formulation, the capacity curves for each structure were obtained. As expected, the introduction of GO improved the performance of the structures. Therefore, from this starting point, depending on the new performance characteristics of the tested formulations (i.e., G30a, G30b, and G30c), efforts were made to decrease the dimensions of the columns and beams (i.e., cross-sections) while maintaining a similar mechanical response for each model, as evaluated in terms of their capacity curves.

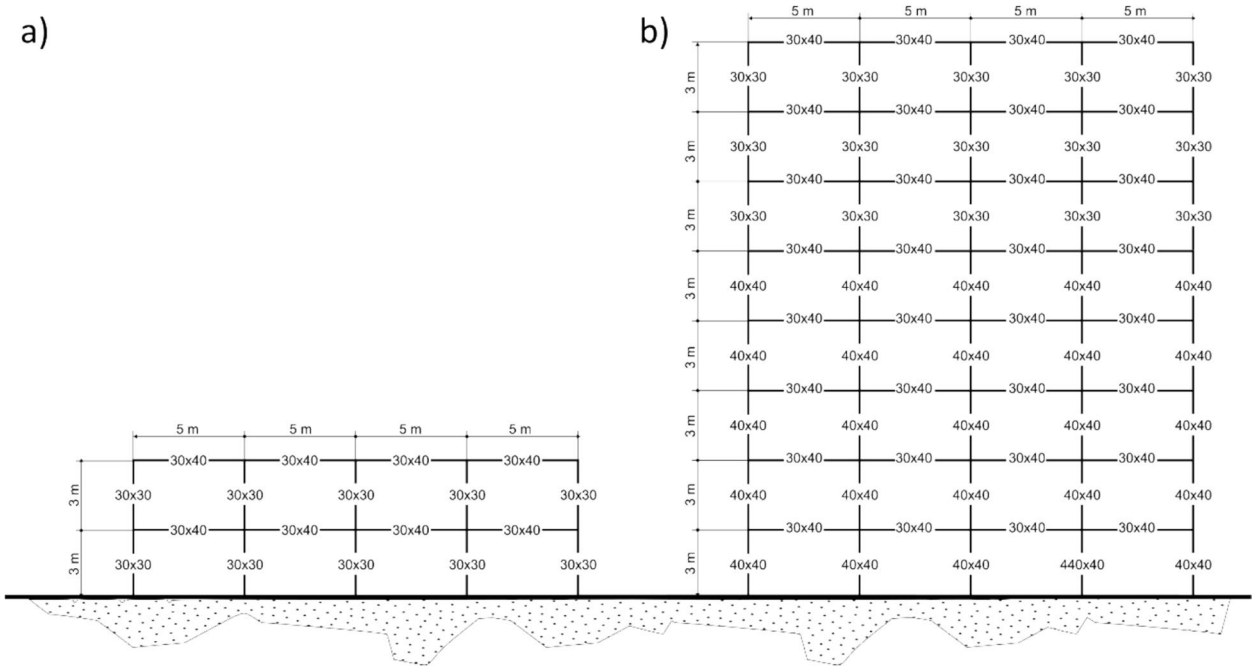

Fig. 5 Portal frame structure: dimensions and sections used (heights in m and section elements (beams and columns) in cm). **a**) Case for two-story and **b**) case for eight-story

The calculation system used in the modelling was based on the finite element analysis method (Aycardi et al., 1992). For the structural analyses conducted in this research, distributed inelasticity elements were employed. This type of element is increasingly used in seismic engineering applications, both in academic research and professional practice. Authors such as Filippou and Fenves (2004), and Fragiadakis and Papadrakakis (2008), have conducted detailed studies highlighting the advantages of distributed inelasticity models compared to simpler concentrated plasticity models. One of the main advantages of this approach is that it eliminates the need for calibrating empirical response parameters based on the actual or idealised behaviour of a frame element under specific loading conditions, as is required in concentrated plasticity models.

The software used in this research, SeismoStruct®, employs a fibre-based modelling approach to represent the behaviour of cross-sections. Each fibre is associated with a uniaxial stress–strain relationship and the sectional stress–strain state of beam-column elements is obtained by integrating the nonlinear uniaxial stress–strain response of the individual fibres (typically 100–150 fibres).

Each structural element (columns and beams) was modelled following the prescriptions proposed in the bilinear model of Mander (Bosco et al., 2016) for concrete and Ferrara (Calabrese et al., 2010) for structural steel. Furthermore, columns and beams were represented as nonlinear bar finite elements. The nonlinearity of the structural elements was concentrated in 'plastic hinges' (European Committee for Standardization, 1992). In the areas near the connections of these elements, the connections between the different structural elements were rigid, in accordance with Scott and Fenves (Aycardi et al., 1992). The advantage of this formulation is not only the reduction of analysis time but also the total control and calibration of the length of the plastic hinges, thus mitigating the challenges associated with their location, as described by Calabrese et al. (2010) (Inel & Ozmen, 2006). In this case, the location of these hinges or the nonlinearities of the structural elements was concentrated at a distance equivalent to 10% of the total length of the element (Salehi & Sideris, 2020).

Moreover, to conduct this analysis, it is necessary to define the number of fibres utilised in the calculation of the balance performed in the extreme sections of the element. The ideal number of fibres needed to sufficiently ensure adequate representation of the stress–strain distribution in the element section varies with material properties and shape, and also depends on the degree of inelasticity which the element is expected to endure. In this case, to determine these models, sections with 300 fibres were defined and damping was defined by

coefficients calculated from the Rayleigh damping matrix (Mergos & Kappos, 2015).

The tolerances used for displacements and rotations were of the order of $10^{\wedge -5}$ in both cases, with a maximum number of 300 iterations. Meanwhile, standard values were used for the unit strains, corresponding to the failure processes of concrete and steel in the SeismoStruct software, namely concrete cracking (0.0001), concrete spalling (−0.002), concrete failure (−0.0020), creep (0.0025), and steel fracture (0.0600). Material deformations were modelled following the classical laws of elasticity; curvature and rotation criteria were verified through the rotation capacity of Mergos and Kappos (European Committee for Standardization, 1998), while shear capacity was established in Eurocode 8 (Hong et al., 2022). Finally, to determine the behaviour of the frame elements, a classic finite element formulation based on displacement was used (Dong et al., 2024).

Push-over analysis was used to estimate the maximum horizontal capacity of structures involved in the dynamic response of the structure that were not significantly affected by the levels of deformation experienced. The incremental load, P, applied at each floor was proportional to the nominal load pattern (P°), where $P=\lambda(P^{\circ})$. To determine these calculations, the SeismoStruct program (Scott & Fenves, 2006) was used. This program automatically increases the load factor, λ, until a limit defined by the user is reached or numerical instability occurs. In these analyses, a triangular load pattern was used.

2.6 Economic Assessment

The economic analysis of the proposed cases was based on the costs associated with concrete and GO, along with the price of CO_2 credits, as the carbon footprint of each resulting structure would be controlled by the total volume of concrete and GO used. As the aim of this study is to compare the effects of different concrete formulations with similar mechanical properties, the functional unit is the production of one building. The barriers include all aforementioned costs during the entire construction process. However, the operational phase and end-of-life or recycling procedures were not considered because of the lack of available information in this regard (Fig. 6). Thus, the overall cost for each case (i) was calculated as follows (Eq. 5):

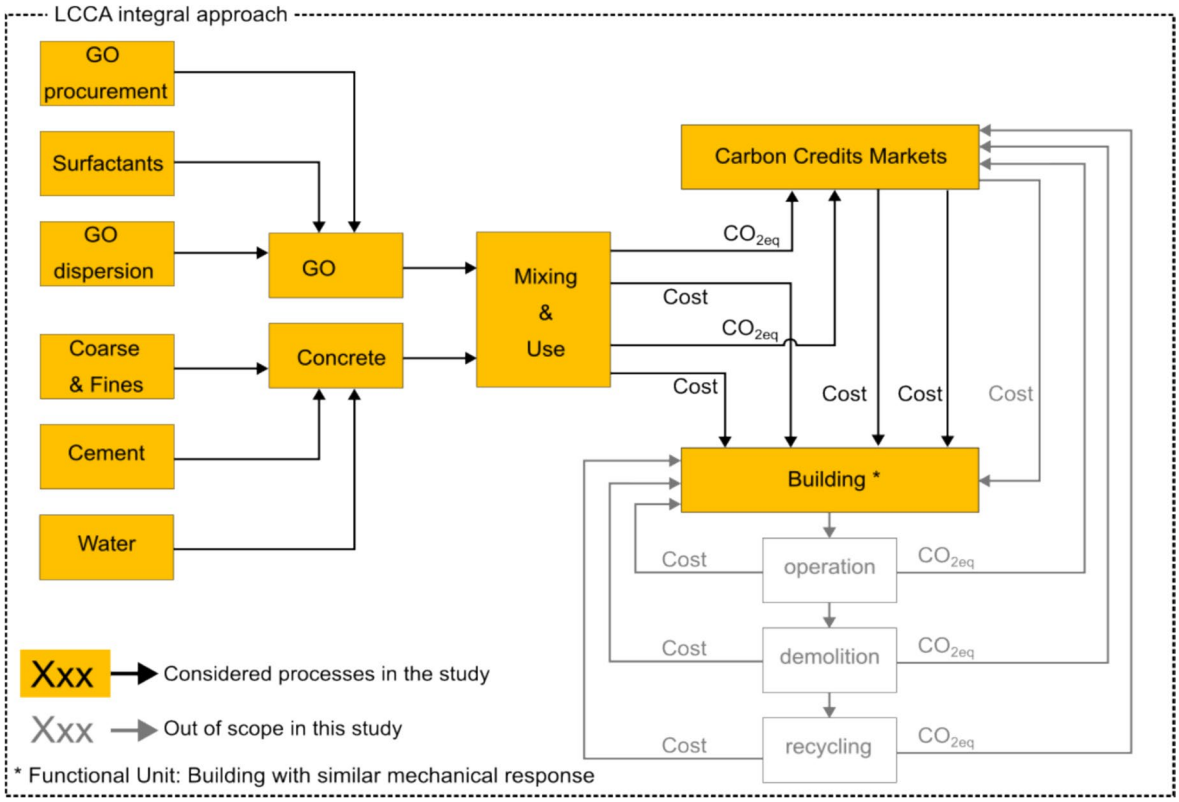

Fig. 6 Life cycle cost analysis (LCCA) and system boundaries of the study

$$C_i = \left[(V_i \cdot \alpha) + \left(GO_i \cdot \beta_j\right)\right] + \left[(V_i \cdot a) + (GO_i \cdot b)\right] \cdot \gamma_k \quad (5)$$

where V_i and GO_i are the total quantities of concrete [m^3] and GO [kg], respectively accounted for buildings in each case under study (i.e., i = G30,G30a,G30b, and G30d). α is the cost of concrete [€/m^3], β_j is the cost of GO, depending on the scenario considered (i.e., j = 50, 100, 150, and 250 €/kg), and γ_k is the price of the $CO_{2,eq}$ credit, depending on the scenario (i.e., k = 60, 100, 150, and 200 €/Ton). Finally, a and b are the emissions per unit of concrete [$TonCO_{2eq}/m^3$] and GO [$TonCO_{2eq}$/kg], respectively.

Regarding the costs of the concrete and GO, the base prices were set at 60 €/m^3 and 250 € per kg for concrete (Rady et al., 2024) and GO, respectively (Warner et al., 2013a). Clearly, the economic viability of GO-enhanced concrete is directly influenced by production costs, scalability, and market incentives such as carbon credits. Graphene materials, including GO, reduced graphene oxide (rGO), and graphene nanoplatelets (GNPs), exhibit distinct cost structures due to their synthesis methods and applications. Historically, GO production has been limited by high costs, primarily due to energy-intensive methods such as chemical vapour deposition (CVD) and the challenges of achieving high-quality, defect-free material.

However, advancements in production technologies are driving costs down. For example, roll-to-roll synthesis and improvements in liquid-phase exfoliation have demonstrated the potential for scalable and cost-effective production of GO, with some projections indicating that graphene production costs could fall to $10–15 per kg in the near future (Warner et al., 2013b). GO, produced via methods such as the modified Hummers process, is one of the most economical options at an industrial scale, with production costs between $100 and $500 per kg, depending on scale and purity (Lin et al., 2019; Tallentire, 2022; Warner et al., 2013b). Although the current cost of GO still is around 5 to 10 times higher than cement, based on the latest advances (i.e., in terms of production methods, scalation, growing markets and suppliers), many issues related to GO synthesis have been resolved, lowering the cost of its preparation (Nazarpour & Waite, 2016). Therefore, the reference price for GO was set at €250 but three more price scenarios were also studied by considering a reduction of GO cost, to €150, €100, and €50 per kg.

The feasibility of GO-enhanced concrete is also tied to the global carbon credit market. As governments and industries prioritise carbon neutrality, the value of CO_2 credits has risen, providing economic incentives for adopting sustainable technologies like GO-enhanced concrete. For instance, the carbon offset potential of using GO to reduce material consumption and enhance durability in construction aligns well with current market trends favouring green building practices.

At this point, in relation to concrete production, the CO_2 equivalent footprint ($CO_{2,eq}$) typically ranges from 302 to 655 kg $CO_{2,eq}/m^3$ (Griffiths et al., 2023). On the other hand, with a focus on GO, although the environmental impact of GO has scarcely been studied, some studies may be highlighted. Arvidsson (Arvidsson, 2017) and Serrano-Luján et al. (Serrano-Luján et al., 2019) provided useful insights into the production of GO through different pathways. Although these studies showed some discrepancies, both agreed that electricity generates the biggest environmental impact, with the cumulative energy demand for GO production ranging between 20.7 and 68.5 GJ per kg of GO. Therefore, these values can be transferred into $CO_{2,eq}$ units by considering the average emission factors. In this regard, this study utilised the findings of Li et al. (Li et al., 2023), who reported an average of 0.2 tonne $CO_{2,eq}$ per MWh.

Over the past decade, the price of CO_2 in global markets has shown a significant upward trend, driven by increasing regulatory measures and a growing commitment to reducing greenhouse gas emissions. The implementation of carbon pricing mechanisms, such as carbon taxes and emissions trading systems (ETS), has been a key factor in this evolution. From 2013 to 2023, the average global price of carbon has risen from approximately 5 € per ton to around 60 € per ton. This increase reflects the expanding coverage of carbon pricing initiatives, which now span 49 advanced and emerging market economies, more than double the number from a decade ago (International Monetary Fund, 2023). The European Union's Emissions Trading System (EU ETS) has been particularly influential, with prices reaching over €90 per ton in 2023, up from less than €10 per ton in 2013 (Luna-Romera et al., 2024). Hence, based on the current trends and market dynamics and adding to the basis analysis (i.e., CO_2 prices of 50 € per ton), three more possible scenarios for the future evolution of CO_2 prices can be outlined.

- *Steady Increase Scenario* In this scenario, CO_2 prices continue to rise steadily, reaching $150 per ton by 2050. This assumes ongoing policy enhancements and gradual economic growth, with countries progressively tightening their carbon pricing mechanisms to meet climate targets.
- *Accelerated Increase Scenario* Here, CO_2 prices rise more rapidly, reaching $200 per ton by 2050. This

scenario assumes a stronger global commitment to climate action, with significant policy shifts and higher carbon taxes or stricter ETS caps being implemented to accelerate emissions reductions.

– *Stabilisation Scenario* In this scenario, CO_2 prices stabilise at around $100 per ton by 2050. This assumes that current policies remain largely unchanged, with moderate economic growth and incremental improvements in carbon pricing mechanisms.

These scenarios highlight the potential range of CO_2 price trajectories, influenced by various economic, political, and environmental factors. Understanding these trends is crucial for assessing the economic feasibility of GO-enhanced concrete and other carbon-intensive technologies.

3 Results and Discussion

3.1 GO Characterisation

Surface chemical information and the identification of oxygen-bearing functional groups in the GO sample were obtained by XPS. Fig. 7 is a broad energy scan spectrum, predominantly showing the presence of oxygen (O 1 s, O 2 s) and carbon (C 1 s). The photoelectron signals from potassium (K 2p, K 2 s) and sodium (Na 1 s) are impurities attributed to the oxidising agents used in the GO synthesis. The signal from the aluminium (Al 2p and 2 s) is from the Al substrate used to deposit the GO sample on the XPS holder.

The presence and identification of the oxygen functional groups present in the GO sample were studied by curve fitting of the high-resolution C 1 s XPS signal (Fig. 8). The peak centred at 284.8 eV and corresponds to the presence of the C–C and C=C bonds from the graphene hexagonal structure. The other de-convoluted peaks, centred at 286.7, 287.1, and 288.6 eV, can be attributed to the oxygen-bearing functional groups associated with CO/COH (epoxy and hydroxyl), C=O (carbonyl) and COOH/COO- (carboxyl and carboxylate), respectively (Krishnamoorthy et al., 2013).

Fig. 9 shows a Raman spectrum acquired from the GO sample. This spectrum displays the characteristic D and G bands at 1358 and 1603 cm^{-1}, respectively. Additionally, broad and weak 2D, D+G, and 2D´ bands are observed at around 2714, 2938, and 3170 cm^{-1}, respectively. The D band is related to a breathing mode from the sp2 carbon rings near a graphene edge or a defect. On the other hand, the G band corresponds to the in-plane vibrational mode of the sp2 hybridised carbon atoms (Cuong et al., 2010). The IG/ID ratio between the intensities of the G and D bands is generally used to quantify the defects present in the graphene-like sheet of the GO structure. For this sample, the IG/ID ratio was 1.01 ± 0.01, suggesting that the oxidation and exfoliation process of the initial graphite resulted in the insertion of

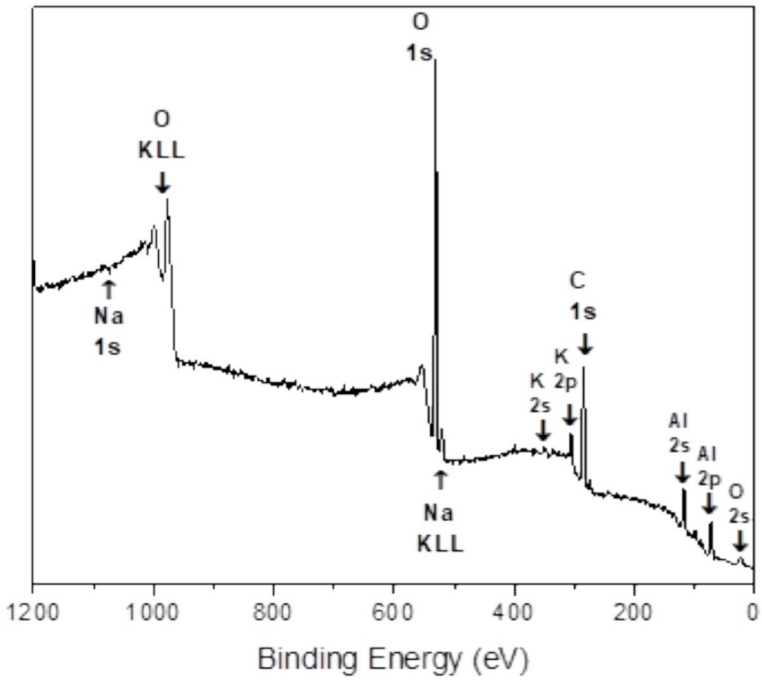

Fig. 7 XPS survey spectrum acquired from the GO sample

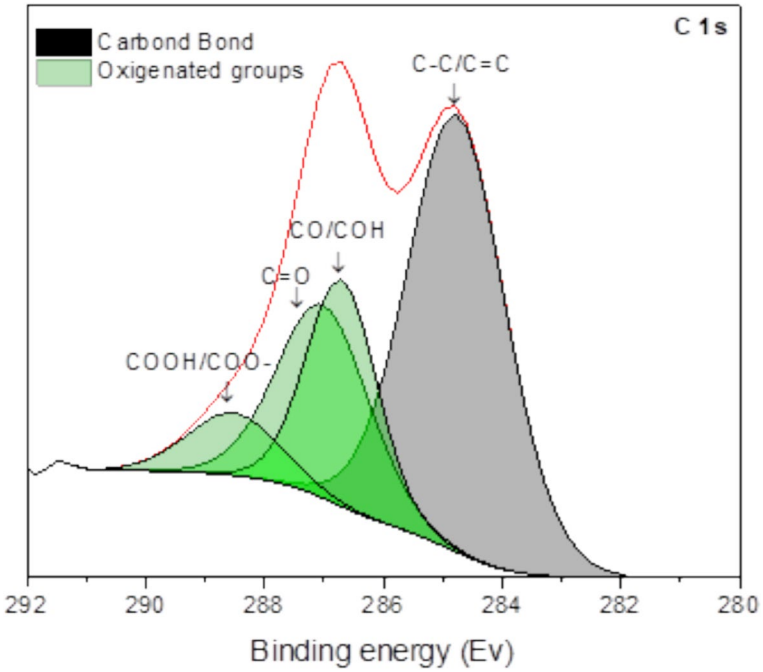

Fig. 8 High resolution XPS spectrum of the C 1 s photoelectron signal acquired from the GO sample

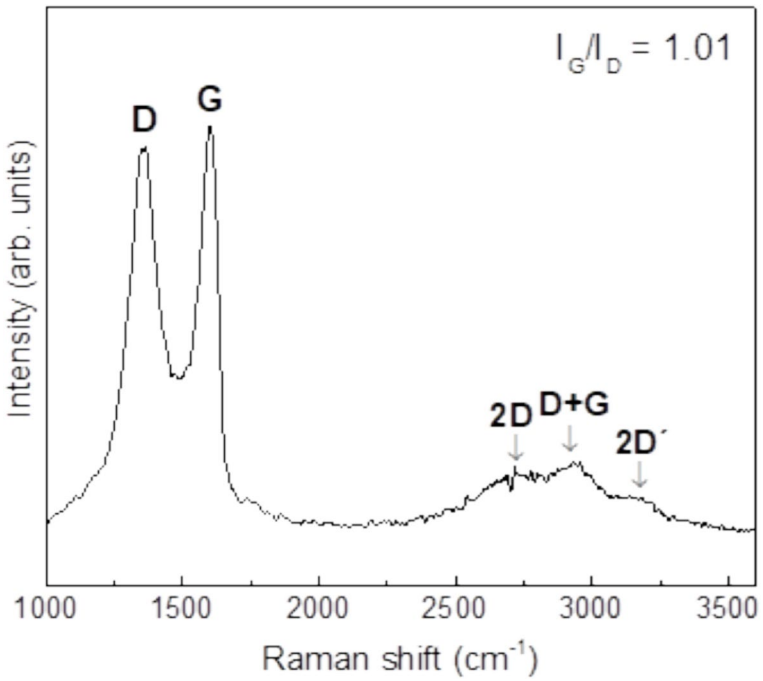

Fig. 9 Raman spectrum obtained of the synthesised GO sample

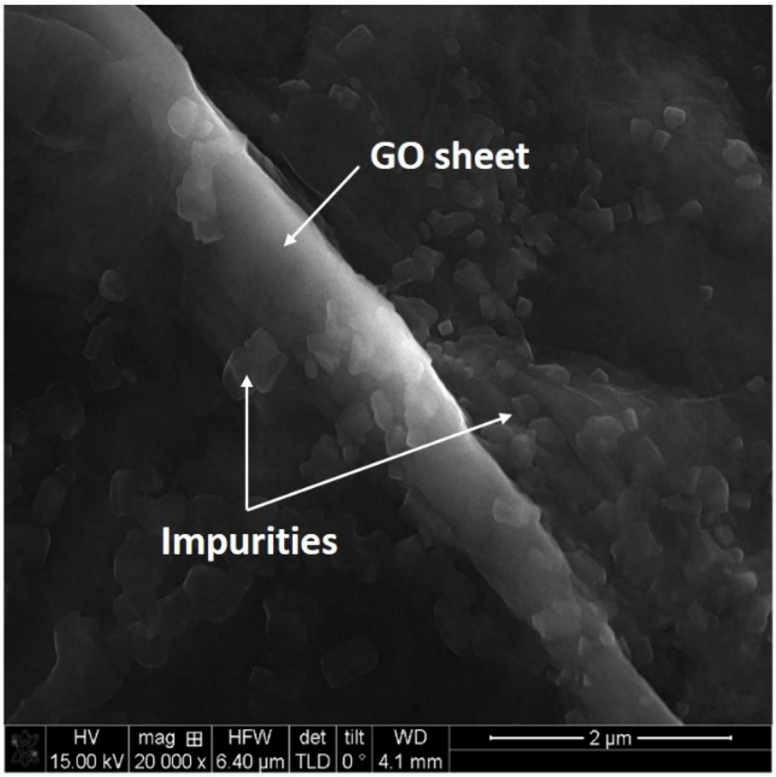

Fig. 10 SEM image obtained of the synthesised GO sample

the oxygen functional groups, thus destroying the layered graphitic structure and leading to the formation of GO sheets' detectable defects. The strong D band, along with the partial suppression of the D + G band in the Raman spectrum, is associated with the loss of conjugated carbon bonds in the GO sample. For comparison, the value of the IG/ID ratio in highly crystalline pristine graphite is approximately 6 times greater than the presently obtained ratio, a result of the G band being much more intense than the D band (Cuong et al., 2010).

Fig. 10 shows an SEM image acquired from the synthesised GO sample, with an average length of approximately 50 µm. The image reveals a rolled-up GO sheet containing particles of impurities, as indicated by the arrows in the image. As revealed by the XPS survey,

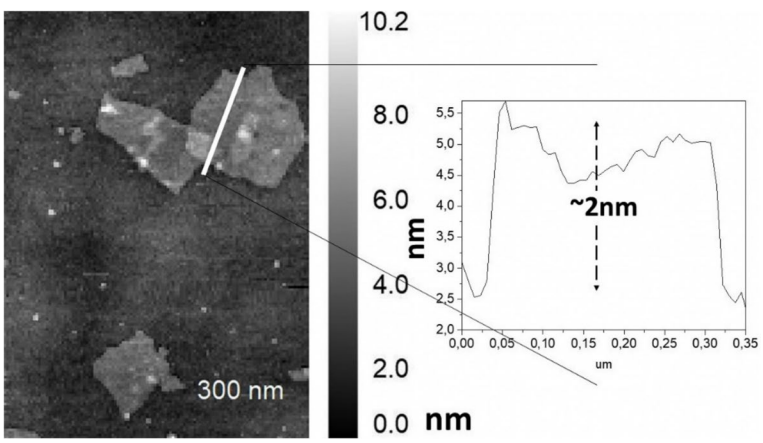

Fig. 11 AFM image (left) and height of AFM profile from a single GO sheet (right)

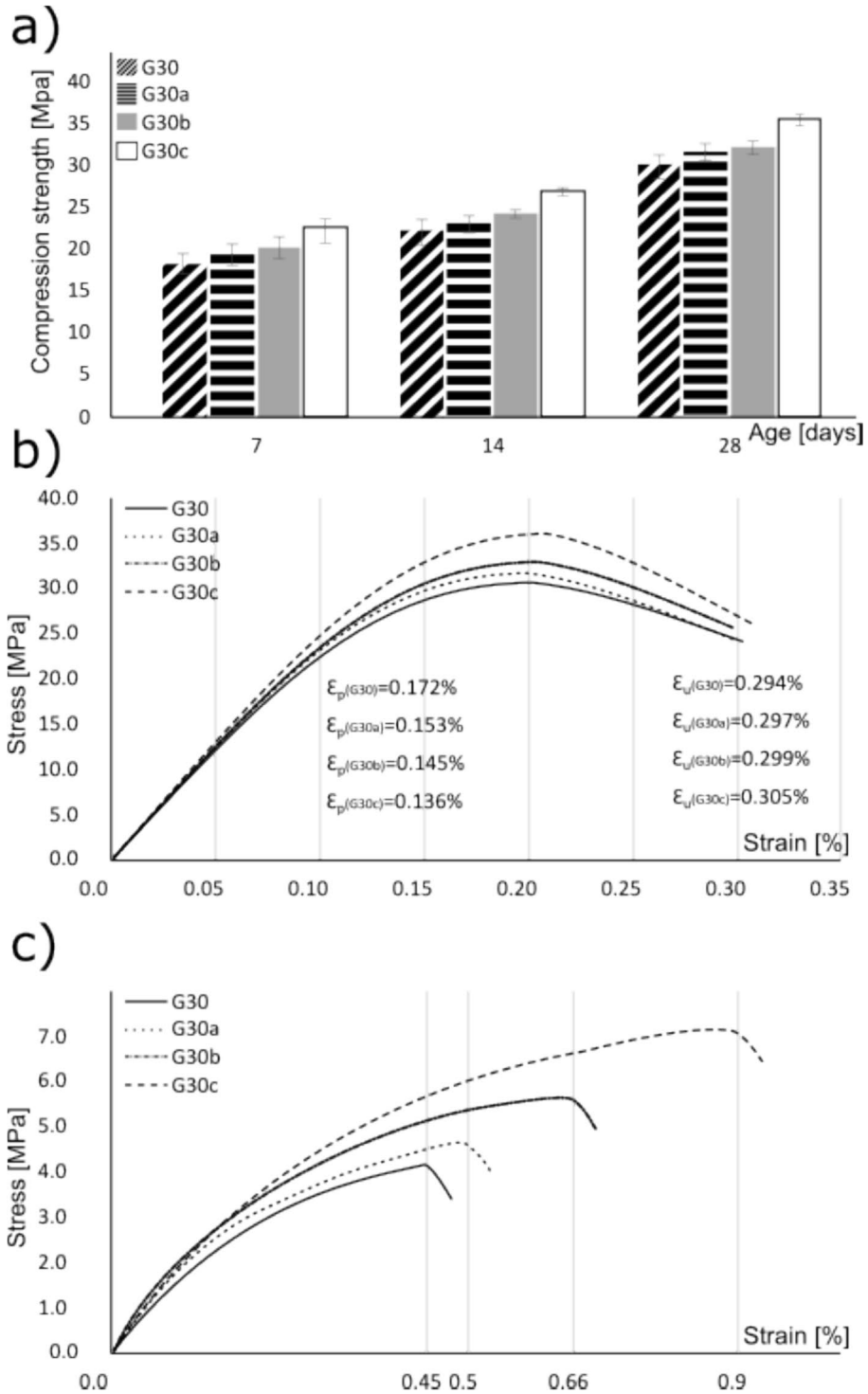

Fig. 12 **a** Ultimate compressive strength as a function of GO addition and age. **b** Average stress–strain curve from uniaxial compression testing at 28 days. **c** Average stress–strain curve from flexural testing at 28 days

the GO sample contains impurities from the oxidising agents used in the synthesis.

For a more detailed study of the morphological characteristics of the GO sheets, AFM was performed. Fig. 11 (left) shows GO sheets of different sizes deposited on a Si substrate for this analysis, while Fig. 11 (right) displays an AFM height profile from the indicated GO sheet. The thickness of a single GO layer, as measured by AFM, was determined to be approximately 2 nm, which contrasts with the theoretically expected thickness of 0.4 nm for a graphene layer (Geim & Novoselov, 2007). Therefore, the AFM profile corroborates the presence of single GO sheets. The thickness of the GO is due to the oxygen functional groups attached to the basal plane of the GO structure, as well as the possible presence of water molecules adsorbed on the surface (Loh et al., 2010).

3.2 Sample Characterisation

The samples with small doses of GO show increased mechanical properties relative to traditional concrete. The compressive strength of the GO concrete increased by 4.8%, 7.70%, and 17.92% for 0.05, 0.10, and 0.20 wt.% content in cement, respectively (Fig. 12a). These values are notably higher than previous results for equal concentrations of GO. Devasena and Karthikeyan (Devasena & Karthikeyan, 2024) reported strength increases of 3%, 9%, and 8% for 0.05, 0.10, and 0.20 wt.% GO in cement, respectively. These differences may be explained by the water-to-cement ratio. As mentioned, there are two main reasons for the improvement in strength: the acceleration of the hydration process of the cement and the filler effect of GO (Cao et al., 2016). Therefore, the rearrangement of particles within the cementitious matrix and the hydration process largely depend on the water-to-cement ratio, as demonstrated by Preethi and Chikkanagoudar (Preethi & Chikkanagoudar, 2019). These authors highlighted that, for the same concentration of GO, increasing the water-to-cement ratio results in a reduction of the average strength. For instance, for 0.03 wt.% GO, the compressive strength increased by 4.8% and 14.9%, for water-to-cement ratios of 0.5 and 0.4, respectively (Preethi & Chikkanagoudar, 2019). Similar results were observed by Qureshi et al. (Dhemla et al., 2022), related to compressive strength; they showed an increase of approximately 30% for 0.16 wt.% GO at 28 days.

The same principle can be applied to the discrepancies in flexural strength (Fig. 12c). In this study, the flexural strength increased relative to traditional concrete and was measured as 13.93%, 39.30%, and 74.78% for 0.05, 0.10, and 0.20 wt.% GO in the cement, respectively (Table 2). Between 0.04 and 0.06 wt.% GO, a 20% average increase in flexural strength was reported by Yeke and Yu (Yeke & Yu, 2021).

As already discussed, the introduction of GO into concrete not only increases the ultimate strength but also the elastic modulus. This leads to an increased ability of the concrete to absorb strain energy, resulting in improved ductility (Horszczaruk et al., 2015). In this study, this trend has been confirmed from the stress–strain curves (Fig. 12b). The modulus of elasticity slightly increases with increasing GO contents (Table 2), in agreement with previous studies (i.e., the results showed that the range of 0.01–0.05% GO increased the elastic modulus from 15.08 to approximately 25 GPa) (Hau Hong et al., 2020).

Although the elastic modulus of porous materials is widely accepted to decrease with a reduction in porosity (Reddy & Prasad, 2023), in this study, the density of the GO concrete is slightly less than the control samples (Table 2). Several investigations show that GO contributes to a more compact and interconnected microstructure, minimising the presence of voids and increasing the density of the cementitious matrix (Fonseka et al., 2023). However, it must be noted that concrete is a heterogeneous material with inherent uncertainties, which may explain these observations (Farooq et al., 2021). Furthermore, some authors have shown that the density of samples containing GO varied by less than 2% within the same GO concentration ranges investigated in this study (Wang et al., 2017). Nevertheless, the slight reduction of bulk density observed may be attributed to higher rates of water loss under natural curing conditions, driven by the accumulation of heat during hydration, which intensifies the loss of free water (Wang et al., 2023).

Table 2 Results from the flexural testing

ID	E [GPa]	Density [kg/m^3]	Compression strength [MPa]	$\varepsilon_{y\,[-]}$	Flexural strength [MPa]	Ductility [-]
G30	21.66	2356	30.09	0.00138	4.02	1.71
G30a	22.30 (+3.0%)*	2334 (– 0.9%)*	31.48 (+4.6%)*	0.00141 (+2.2%)	4.58 (+13.9%)	1.94 (+13.5%)
G30b	23.17 (+7.0%)*	2324 (– 1.4%)*	32.31 (+7.4%)*	0.00139 (+0.7%)	5.60 (+39.3%)	2.06 (+20.5%)
G30c	24.43 (+12.8%)*	2301 (– 2.3%)*	35.38 (+17.6%)*	0.00145 (+5.1%)	7.06+75.6%)	2.25 (+31.6%)

*In parentheses, value expressed as a percentage of improvement or deterioration relative to the control value

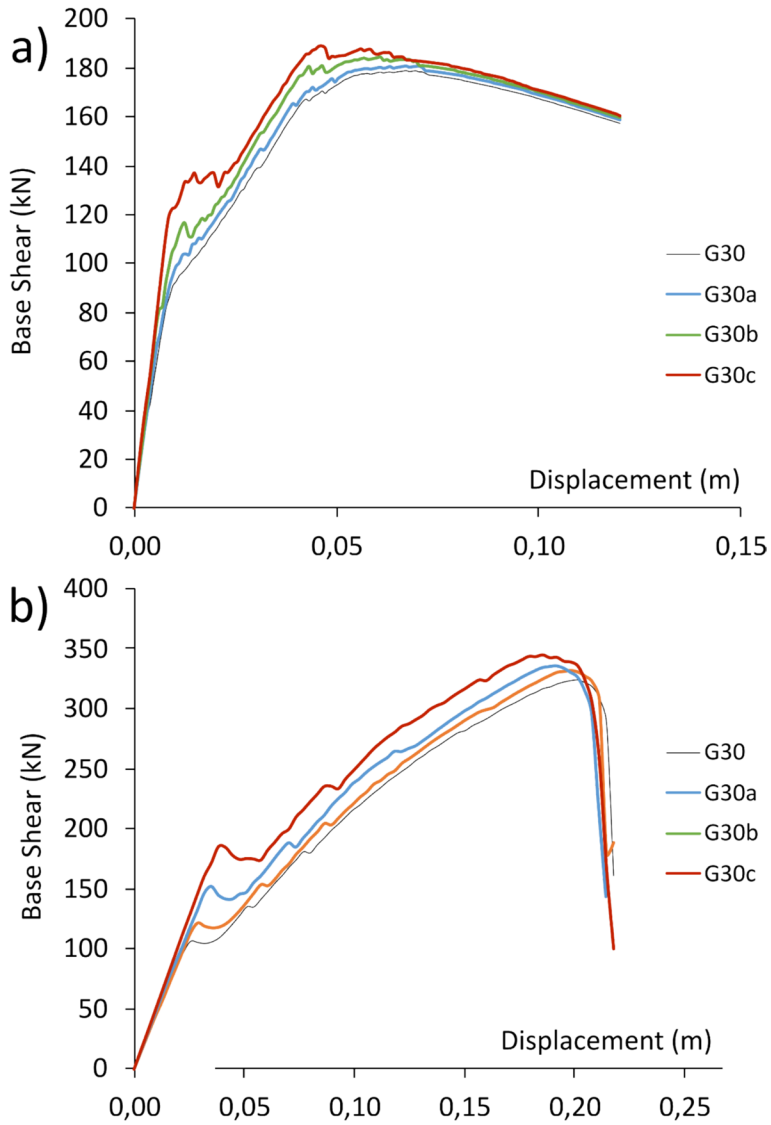

Fig. 13 Capacity curves for **a**) two-story and **b**) eight-story structures with the same structural cross-section in all cases

3.3 Building´s Mechanical Response

The capacity curves obtained from the push-over analyses are shown in Figs. 13 and 14. The most significant results from the capacity curves shown in Fig. 13, where the same structural sections were used, indicate progressive increases in plastic strength (between 2 and 8%) and ultimate strength (between 2 and 7%) of the frames as the amount of GO increases. On the other hand, the plastic deformation (ranging from 6 to 23% for 2-storey frames and from 2 to 16% for 8-storey frames) and ultimate deformation (ranging from 9 to 32% for 2-storey frames and from 2 to 9% for 8-story frames) of the frames decreases as the amount of GO increases.

Regarding ductility, in the case of 2-storey frames (Fig. 13a), no clear relationship can be established with the amount of GO. However, ductility progressively increases in taller frames, ranging from 4 to 10% (Fig. 13b).

Based on the properties of the new GO-enhanced concrete formulations, the structures have reduced their cross-sections as indicated in Tables 3 and 4.

For Fig. 14, where the strengths of the frames are similar, it can be observed that, increasing the GO content

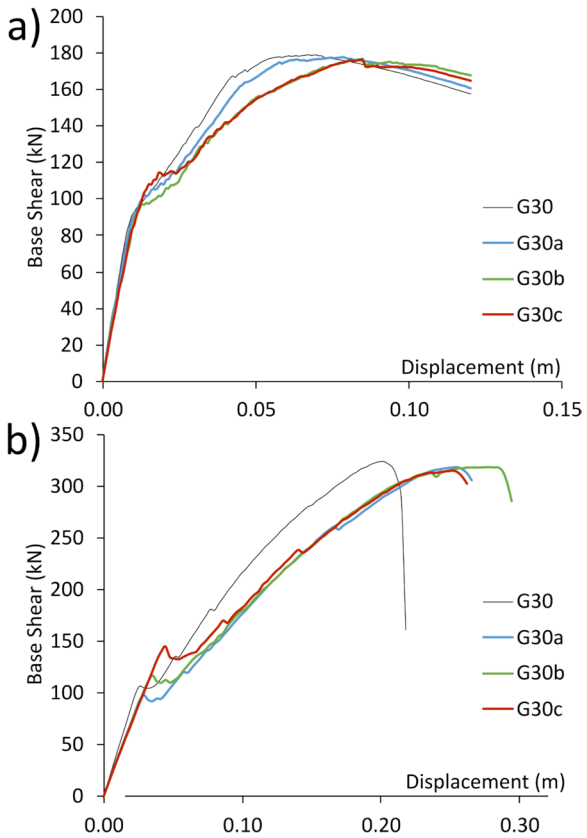

Fig. 14 Capacity curves for **a**) two-story and **b**) eight-story optimized structures with similar strength and different structural cross-section

Table 3 Resulting sections of the structure for a similar mechanical response for each case in a two-storey frame

	G30	G30a	G30b	G30c
floor_1 columns	30×30 cm^2	30×30 cm^2	30×30 cm^2	30×25 cm^2
floor_1 beams	30×40 cm^2	30×35 cm^2	30×30 cm^2	30×30 cm^2
floor_2 columns	30×30 cm^2	30×30 cm^2	30×30 cm^2	30×25 cm^2
floor_2 beams	30×40 cm^2	30×35 cm^2	30×30 cm^2	30×30 cm^2

Table 4 Resulting sections of the structure for a similar mechanical response for each case in a two-storey frame

	G30	G30a	G30b	G30c
floor_1 to 4 columns	40×40 cm^2	40×40 cm^2	40×30 cm^2	40×25 cm^2
floor_1 to 4 beams	30×40 cm^2	30×35 cm^2	30×35 cm^2	30×35 cm^2
floor_5 to 8 columns	30×30 cm^2	30×30 cm^2	30×30 cm^2	30×25 cm^2
floor_5 to 8 beams	30×40 cm^2	30×35 cm^2	30×35 cm^2	30×35 cm^2

in the mixtures leads to section reductions. For the case G30a, beam heights are reduced by 5 cm (from 30×35 cm^2) and for G30b, beam heights are reduced by 10 cm (to 30×30 cm^2) and column heights by 5 cm (to 30×25 cm^2). In the case of 2-storey frames, beam heights are reduced by 10 cm (to 30×30 cm^2).

For 8-storey frames, beam heights are reduced by 5 cm (to 30×35 cm^2) with G30a. For G30b, the lower four floors' column sections are reduced by 10 cm (to 30×40 cm^2) and beam heights by 5 cm (to 30×35 cm^2). For G30c, column sections are reduced by 15 cm on the lower four floors (to 25×40 cm^2), by 5 cm on the upper four floors (to 30×25 cm^2), and beam heights are reduced by 5 cm (to 30×35 cm^2). The results show that small amounts of GO in the production of concrete improve the structural properties of the frames, in agreement with other research (Monteiro et al., 2017; Salami et al., 2023). The properties that improve most significantly are flexural strength (76%) and ductility (32%), which are also the most deficient characteristics in traditional concrete. This is where the effectiveness of GO as a semi-metal in a highly fragile material, such as concrete, becomes effective.

Moreover, it is evident that reducing the concrete density leads to a decrease in the seismic forces of the models (Vandanapu & Krishnamurthy, 2018; Xue & Shinozuka, 2013). At the bottom of each case, the percentages of total seismic force relative to traditional concrete (G30) are shown. The reduction in percentage is 91%, 83% and 76% for G30a, G30b and G30c, respectively, for the two-storey example. These values are consistent across both models; thereby, in the case of the eight-storey building, reductions of 92%, 85% and 78% were determined for G30a, G30b and G30c, respectively. This calculation methodology has been successfully used to determine the seismic calculation forces that are used for any structural design, particularly in highly seismic locations (European Committee for Standardization, 1992). Determining seismic forces across various types of existing soil is of broader international relevance, given the varying effects of earthquakes on buildings. This is evident in the catastrophic effects that occur in areas with soft soils whenever a medium-magnitude earthquake occurs (UNAM Seismology Group, 2015).

The reduction in base shear for each type of soil, compared to traditional concrete, compared with the various concretes containing GO, can be obtained from Tables a1 and a2 (see appendix a). Thus, seismic force reductions range from 8 to 24% in cases where GO is added to the new mixtures.

The reduction in weight in structures is essential, to optimise their strength and efficiency. By decreasing the

load they must bear, their durability and lifespan can be increased (Sun et al., 2024). Furthermore, by reducing the weight of the structures, material consumption is lowered, which results in a positive environmental impact.

There are various strategies to reduce weight in structures, such as using lighter and stronger materials, designing more efficient shapes, and eliminating unnecessary elements. The application of innovative technologies, such as the use of composite materials or topological optimisation, can also significantly contribute to weight reduction in structures.

In summary, optimising the strength of structures by reducing weight is key to improving their performance and efficiency. By implementing design and construction strategies that reduce the load they must bear, more durable, sustainable, and resilient structures can be obtained. Additionally, reducing the weight of structures can also result in significant savings in material and labour costs (Zareef, 2010).

The reduced weight of materials used in the construction of structures has a significant impact on their efficiency (Sun et al., 2024). By decreasing the total load supported, the stress and fatigue of materials are reduced, which prolongs their lifespan and decreases maintenance costs. Moreover, using lighter materials optimises resource consumption and facilitates the transportation and installation of the structures, contributing to greater sustainability and efficiency in construction. In summary, reduced weight not only improves structural efficiency but also has a positive impact on the economy and the environment.

As mentioned earlier, Tables a1 and a2 (see appendix a) show how seismic forces (and therefore base shear) are reduced by 8–24%, depending on the amount of GO in the concrete. These percentages of seismic force reduction are quite similar between the 2-storey and 8-storey frames. Since they depend on the weight of the structures, the percentage ratios of seismic force reductions for the different soil types remain consistent across all cases. As observed, seismic forces increase as the soil becomes softer, as these scenarios are less favourable in their structural behaviour.

Regarding the results obtained from the seismic forces using the European Seismic Design Code (EC-8), the reduction in the densities of the concretes as GO is added in the preparation of structural sections (beams, columns, and slabs) has a positive effect. This is because seismic forces are related to the weights of the buildings. The reduction in density, as the amount of GO in the concrete composition increases, reduces the weight of the constructions, thereby decreasing the seismic design forces and the base shears of each model, while also reducing the displacements of the structures for different types of soil.

When a triangular load distribution is determined, the highest forces are located on the top floor of each structural model, as shown in Tables a1 and a2 (see appendix a). The reduction in seismic design forces decreases the demand on the structures, reducing the structural sections of the models.

In highly seismic areas, the reduction in seismic forces due to the decreased weight of the structures has significant implications for building safety. Lighter structures experience lower inertial forces during an earthquake, which reduces the overall demand on the structural elements. This can lead to improved performance during seismic events, with reduced risk of structural damage or failure. Additionally, the reduced displacements contribute to the overall stability of the building, minimising the potential for non-structural damage and enhancing occupant safety.

3.4 Economic Feasibility

Table 5 shows the volume of concrete and GO used for each of the analysed cases and the corresponding overall $CO_{2,eq}$ emissions. The reduction in the amount of cement used (i.e., resulting from the reduction in the size of the structural elements) varies by approximately 8%, 15%, and 21%, for additional percentages of 0.5% (G30a), 1.0% (G30b), and 2.0% (G30c), respectively, for both two and eight-storey buildings (Figs. 15 and 16). This reduction proportionally impacts the building's carbon footprint, leading to partial economic savings in all cases. However, the price of GO has a greater influence, in terms of partial cost. Thus, adding small amounts of GO proves to be

Table 5 Summary of resulting amounts of concrete and GO for each building case

ID	Concrete [m^3] two-storey	GO [kg] two-storey	$CO_{2,eq}$ [kg] two-storey	Concrete [m^3] eigth-storey	GO [kg] eigth-storey	$CO_{2,eq}$ [kg] eigth-storey
G30	7.5	–	3,588.8	34.2	–	16,364.7
G30a	6.9	1.41	3,307.7	31.8	6.49	15,244.2
G30b	6.3	2.57	3,025.6	29.4	12.00	14,119.5
G30c	5.85	4.77	2,819.8	27.3	22.28	13,158.9

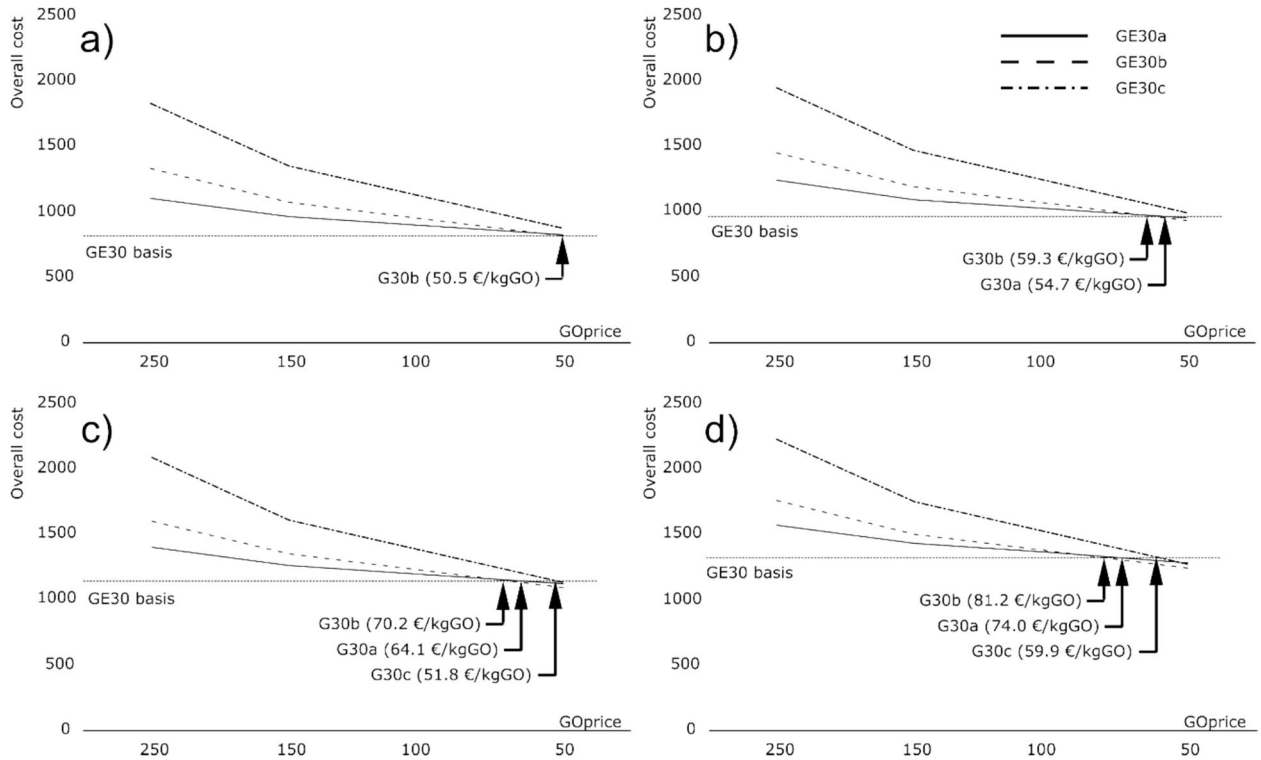

Fig. 15 Overall cost of the two-storey building as a function of the GO price at different scenarios of $CO_{2,eq}$ credit price: **a** 60 €/Ton $CO_{2,eq}$; **b** 100 €/Ton $CO_{2,eq}$; **c** 150 €/Ton $CO_{2,eq}$; **d** 200 €/Ton $CO_{2,eq}$

more economically viable compared to adding larger percentages of GO, since the benefits in terms of CO_2 emissions reduction and improved mechanical properties of the concrete do not fully offset the high cost of GO when used in large quantities.

For both types of buildings (i.e., two- and eight-story), the G30b formulation (0.1% GO) emerges as the most competitive option, as it allows for higher GO prices while still being economically viable compared to traditional concrete (G30). Starting at €60 per tonne of $CO_{2,eq}$, for low-rise buildings (i.e., two-story), a price up to 50 € per kg of GO would allow the replacement of traditional structure by G30b formulations. However, the analysis also reveals that as the building volume increases, the economic scenarios become less favorable for the addition of GO. This is likely due to the higher overall material costs and the diminishing returns on investment in larger structures. Therefore, while G30b is recommended for smaller-scale projects where the benefits of enhanced mechanical properties and reduced $CO_{2,eq}$ emissions can be maximized, its application in larger buildings should be carefully evaluated against the specific economic and environmental goals of the project.

Since the economic feasibility of GO-enhanced concrete largely depends on reducing GO production costs, traditional concrete remains the most economical option across all CO_2 credit price scenarios at the current GO cost. This is because the benefits of reduced CO_2 emissions and improved mechanical properties do not fully offset the high cost of GO. Therefore, for this technology to become viable in the future, advancements in GO production techniques are crucial.

Based on the 2050 target of net-zero emissions, projections suggest that the CO_2 price will increase to between €235 and €280 per tonne of CO_2, according to both the International Energy Agency and the International Monetary Fund. If this price rise is added to the expected reduction in GO production costs, it can be inferred that a CO_2 credit price around €250 and a GO cost below €50 would allow the addition of between 0.05% and 1.0% of GO.

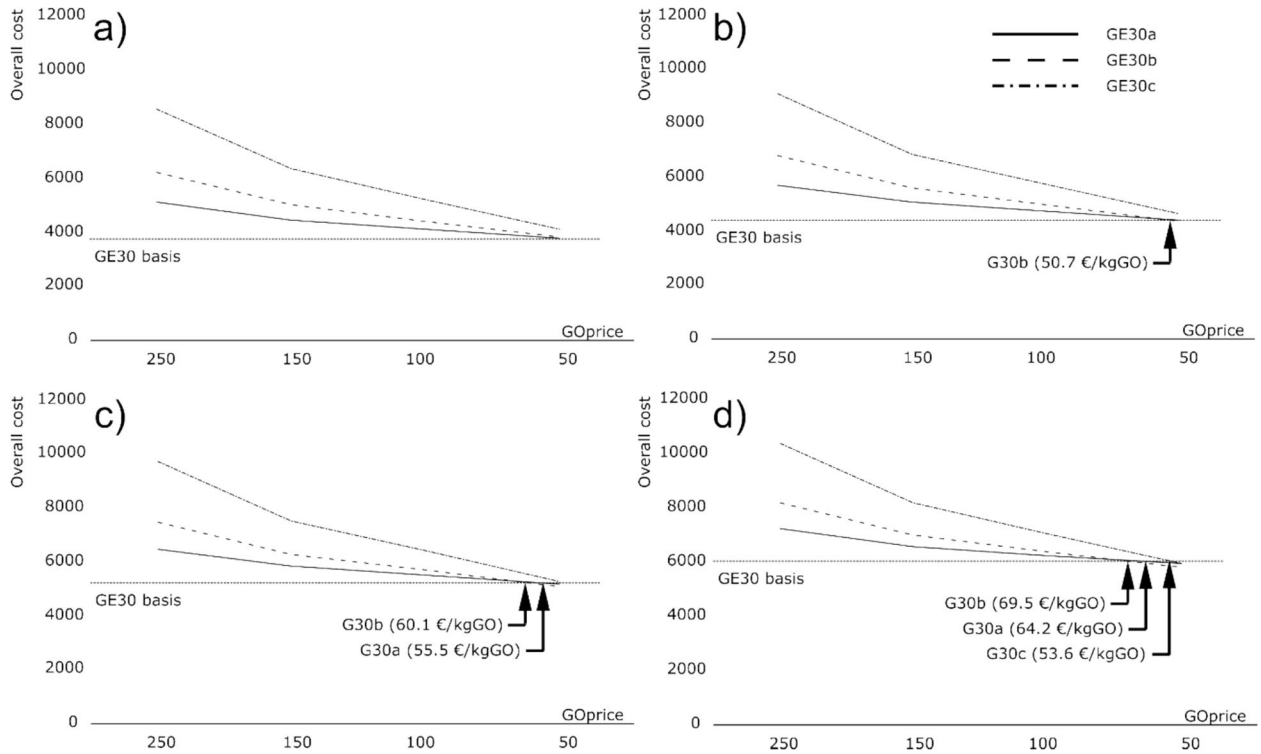

Fig. 16 Overall cost of the eighth-storey building as a function of the GO price at different scenarios of $CO_{2,eq}$ credit price: **a** 60 €/Ton $CO_{2,eq}$; **b** 100 €/Ton $CO_{2,eq}$; **c** 150 €/Ton $CO_{2,eq}$; **d** 200 €/Ton $CO_{2,eq}$

4 Conclusions

This study has successfully demonstrated the techno-economic feasibility of incorporating small quantities of graphene oxide into concrete formulations to produce improved concrete, thereby potentially reducing the required size of structural elements.

The use of graphene oxide -enhanced concrete can be particularly beneficial in regions with high seismic activity, where reducing the seismic demand on structures is crucial. By incorporating lighter and stronger materials, engineers can design more resilient buildings that are better equipped to withstand seismic forces.

By comparing the response of a control building constructed with traditional concrete to those constructed with various proportions of graphene oxide -enhanced concrete, we have demonstrated that the dimensions of the resistant elements can be significantly reduced while maintaining similar structural integrity. Moreover, although the addition of graphene oxide slightly reduces the density of the concrete, the resulting decrease in the size of structural elements significantly reduces the overall weight of buildings.

Furthermore, the reduction in structural section sizes not only improves the seismic performance but also leads to material savings and cost reductions. This aligns with the global trend towards sustainable construction practices, where the focus is on minimising environmental impact while ensuring structural safety and performance.

As a consequence of the reduced weight and smaller structural elements, the seismic forces experienced by buildings are notably diminished (by up to 25%), resulting in lower shear loads. This reduction in seismic forces allows for further optimisation of structural elements, in compliance with building codes and standards, thereby enhancing the overall safety and resilience of the constructed buildings.

Finally, it has also been demonstrated that economic feasibility is inherently dependent on the graphene oxide production cost, while the price of emitted CO_2 credits has a lower influence on the overall cost. Thus,

even in the forecasted scenarios with CO_2 credit prices below €200, a reduction of up to 20–40% in the current average price of graphene oxide would still necessitate factoring in the cost of emitted CO_2 into the overall cost assessment. The use of between 0.05% and 0.10% of graphene oxide would only be justified for a graphene oxide price of around €50/kg.

Additionally, setting the CO_2 credit above €150 per tonne of CO_2eq is essential to enable the economically advantageous incorporation of 0.05% and 0.10% graphene oxide into cement. As governments and industries prioritise carbon neutrality, it is expected that the value of CO_2 credits will continue to increase, providing economic incentives to adopt sustainable technologies like graphene oxide -enhanced concrete. In addition, recent advances in graphene oxide production also lead to a reduction in the cost of graphene oxide.

The adoption of new technologies in construction requires acceptance and support from industry professionals. Thus, it is crucial to demonstrate the long-term benefits of graphene oxide -enhanced concrete, not only in terms of sustainability and structural performance but also in terms of durability, which may reduce economic and environmental impacts along operational and end-of-life stages. Nevertheless, these topics require further research.

Table 6 Seismic forces (kN) according to EC-8 for different types of soil and base shear for each case in a two-storey frame

	Soil A	Soil B	Soil C	Soil D	Soil E
G30_floor_1	4.17	5.63	6.26	9.01	6.68
G30_floor_2	8.34	11.26	12.52	18.02	13.35
Total	12.52	16.90	18.77	27.04	20.03
G30a_floor_1	3.80	5.13	5.70	8.21	6.08
G30a_floor_2	7.60	10.27	11.41	16.43	12.17
Total	11.41	15.40	17.11	24.64	18.25
G30b_floor_1	3.46	4.67	5.19	7.47	5.53
G30b_floor_2	6.91	9.33	10.37	14.93	11.06
Total	10.37	14.00	15.56	22.40	16.59
G30c_floor_1	3.18	4.29	4.77	6.08	5.09
G30c_floor_2	6.36	8.58	9.53	12.17	10.17
Total	9.53	12.87	14.30	18.25	15.26

Table 7 Seismic forces (kN) according to EC-8 for different types of soil and base shear for each case in an eight-storey frame

G30	Soil A	Soil B	Soil C	Soil D	Soil E
G30_floor_1	0.59	0.80	0.89	1.28	0.94
G30_floor_2	1.03	1.39	1.55	2.23	1.65
G30_floor_3	1.48	1.99	2.21	3.19	2.36
G30_floor_4	1.92	2.59	2.88	4.14	3.07
G30_floor_5	2.36	3.19	3.54	5.10	3.78
G30_floor_6	2.80	3.79	4.21	6.06	4.49
G30_floor_7	3.25	4.38	4.87	7.01	5.20
G30_floor_8	3.69	4.98	5.54	7.97	5.90
Total	17.12	23.12	25.68	36.98	27.40
G30a_floor_1	0.54	0.73	0.82	1.17	0.87
G30a_floor_2	0.95	1.28	1.43	2.6	1.52
G30a_floor_3	1.36	1.84	2.04	2.94	2.18
G30a_floor_4	1.77	2.39	2.65	3.82	2.83
G30a_floor_5	2.18	2.94	3.26	4.70	3.48
G30a_floor_6	2.58	3.49	3.88	5.58	4.13
G30a_floor_7	2.99	4.04	4.49	6.46	4.79
G30a_floor_8	3.40	4.59	5.10	7.34	5.44
Total	15.77	21.29	23.66	34.07	25.24
G30b_floor_1	0.50	0.68	0.75	1.08	0.80
G30b_floor_2	0.88	1.18	1.31	1.89	1.40
G30b_floor_3	1.25	1.69	1.88	2.70	2.00
G30b_floor_4	1.63	2.20	2.44	3.51	2.60
G30b_floor_5	2.00	2.70	3.00	4.33	3.20
G30b_floor_6	2.38	3.21	3.57	5.14	3.81
G30b_floor_7	2.75	3.72	4.13	5.95	4.41
G30b_floor_8	3.13	4.22	4.69	6.76	5.01
Total	14.52	19.60	21.78	31.36	23.23
G30c_floor_1	0.46	0.62	0.69	0.99	0.74
G30c_floor_2	0.81	1.09	1.21	1.74	1.29
G30c_floor_3	1.15	1.55	1.73	2.49	1.84
G30c_floor_4	1.50	2.02	2.24	3.23	2.39
G30c_floor_5	1.84	2.49	2.76	3.98	2.96
G30c_floor_6	2.19	2.95	3.28	4.72	3.50
G30c_floor_7	2.53	3.42	3.80	5.47	4.05
G30c_floor_8	2.88	3.88	4.32	6.21	4.60
Total	13.35	18.02	20.02	28.83	21.36

Appendix A

See Tables 6, 7

Acknowledgements
This work is supported by the Chilean National Commission on Research and Development (ANID) [FONDECYT REGULAR grant number 1240156].

Author contributions
P. M.: Conceptualization, Formal analysis, Writing—Original Draft. D. D. S.: Conceptualization, Project administration, Writing—Original Draft. J.O. M-F, C. A. and D.E. D-D.: Data curing**,** Writing—Original Draft. E. V.: Formal analysis**,** Writing—Original Draft.

Availability of Data and Materials
The datasets used and/or analysed during the current study are available from the corresponding author on reasonable request.

Declarations

Competing Interests
The authors declare that they have no competing interests.

Author details
[1]Faculty of Engineering, Universidad de Talca, 3340000 Curicó, Chile. [2]InES Research Group, Universidad Internacional de La Rioja, Logroño, Spain. [3]Faculty of Engineering, Universidad Autónoma de Chile, Talca, Chile. [4]Escuela de Ingeniería, Facultad de Ciencias, Ingeniería y Tecnología, Universidad Mayor, Temuco, Chile. [5]Physics Institute, Physics Faculty, Pontificia Universidad Católica de Chile, Santiago, Chile. [6]Centro de Investigación en Nanotecnología y Materiales Avanzados, CIEN UC, Pontificia Universidad Católica de Chile, Santiago, Chile. [7]Avanzare Innovacion Tecnologica S.L., Av. Lentiscares 4-6, 26370 Navarrete, Spain.

Received: 10 August 2024 Accepted: 7 April 2025
Published online: 25 June 2025

References

Alex, A. G., Kedir, A., & Tewele, T. G. (2022). Review on effects of graphene oxide on mechanical and microstructure of cement-based materials. *Construction and Building Materials, 360*, 129609. https://doi.org/10.1016/j.conbuildmat.2022.129609

Arvidsson, R. (2017). Review of environmental life cycle assessment studies of graphene production. *Advanced Materials Letters, 8*(3), 187–195. https://doi.org/10.5185/amlett.2017.1413

Asem, P., Wang, X., Hu, C., & Labuz, J. F. (2021). On tensile fracture of a brittle rock. *International Journal of Rock Mechanics and Mining Sciences, 144*, 104823. https://doi.org/10.1016/j.ijrmms.2021.104823

Aycardi, L. E., Mander, J. B., & Reinhorn, A. M. (1992). *Seismic resistance of reinforced concrete frame structures designed only for gravity loads: Part II - Experimental performance of subassemblages (Technical Report NCEER-92-0028)*. State University of New York at Buffalo.

Bacatelo, M., Capucha, F., Ferrão, P., & Margarido, F. (2023). Selection of a CO2 capture technology for the cement industry An integrated TEA and LCA methodological framework. *Journal of Utilization*. https://doi.org/10.1016/j.jcou.2022.102375

Balaji, S., & Swathika, A. (2022). Review on mechanical and microstructural properties of cementitious composites with graphene oxide. *Materials Today: Proceedings, 50*(5), 2280–2287. https://doi.org/10.1016/j.matpr.2021.09.544

Bosco, M., Ferrara, E., Ghersi, A., Marino, E. M., & Rossi, P. P. (2016). Improvement of the model proposed by Menegotto and Pinto for steel. *Engineering Structures, 124*, 442–456. https://doi.org/10.1016/j.engstruct.2016.06.037

Calabrese, A., Almeida, J. P., & Pinho, R. (2010). Numerical issues in distributed inelasticity modeling of RC frame elements for seismic analysis. *Journal of Earthquake Engineering, 14*(sup1), 38–68. https://doi.org/10.1080/13632461003651869

Cao, M., Zhang, H., & Zhang, C. (2016). Effect of graphene on mechanical properties of cement mortars. *Journal of Central South University, 23*, 919–925. https://doi.org/10.1007/s11771-016-3139-4

Chung, S.-Y., Kim, J.-S., Lehmann, C., Stephan, D., Han, T.-S., & Abd Elrahman, M. (2020). Investigation of phase composition and microstructure of foamed cement paste with different supplementary cementing materials. *Cement and Concrete Composites, 109*, 103560. https://doi.org/10.1016/j.cemconcomp.2020.103560

Cuong, T. V., Pham, V. H., Tran, Q. T., Hahn, S. H., Chung, J. S., Shin, E. W., & Kim, E. J. (2010). Photoluminescence and Raman studies of graphene thin films prepared by reduction of graphene oxide. *Materials Letters, 64*(3), 399–401. https://doi.org/10.1016/j.matlet.2009.11.029

Devasena, M., & Karthikeyan, J. (2024). Investigation on strength properties of graphene oxide concrete. *International Journal of Engineering Science Invention Research & Development., 307*, 10.

Dhemla, P., Somani, P., Swami, B. L., & Gaur, A. (2022). Optimizing the design of sintered fly ash light weight concrete by Taguchi and ANOVA analysis. *Materials Today: Proceedings, 62*(2), 495–503. https://doi.org/10.1016/j.matpr.2022.03.573

Divya, S., Praveenkumar, S., Akthar, A. S., & Karthiksoundar, N. (2023). Performance variation of graphene nanoplatelets reinforced concrete concerning dispersion time. *Materials Today Proceedings*. https://doi.org/10.1016/j.matpr.2023.05.104

Domínguez, D., López-Almansa, F., & Benavent-Climent, A. (2016). Would RC wide-beam buildings in Spain have survived Lorca earthquake (11–05-2011)? *Engineering Structures, 108*, 134–154. https://doi.org/10.1016/j.engstruct.2015.11.020

Dominguez, D., Muñoz, V. P., & Muñoz, V. L. (2017). Impact of using lightweight eco-bricks as enclosures for individual houses of one story on zones of high seismicity. *Materiales De Construcción, 67*(328), e133. https://doi.org/10.3989/mc.2017.03316

Dong, H., Wang, C., Du, X., et al. (2024). Residual displacement responses of RC bridge columns with degradation and pinching effect under near-fault pulsed ground motions. *Bulletin of Earthquake Engineering, 22*, 3055–3091. https://doi.org/10.1007/s10518-024-01888-y

European Committee for Standardization. (1992). *Eurocode 2: Design of concrete structures - Part 1–1: General rules and rules for buildings*. CEN.

European Committee for Standardization. (1998). *Eurocode 8: Design of structures for earthquake resistance - Part 1: General rules, seismic actions and rules for buildings*. CEN.

de Fomento M. (2008). Instrucción de Hormigón Estructural (Instruction for Structural Concrete) (EHE-08). Madrid: Ministerio de Fomento (Ministry of Public Works).

de Fomento M. (2002). Norma de Construcción Sismorresistente: Parte General y Edificación (Standard for Seismic-Resistant Construction: General Part and Building Construction) (NCSE-02). Madrid: Ministerio de Fomento (Ministry of Public Works).

Farooq, F., Ahmed, W., Akbar, A., Aslam, F., & Alyousef, R. (2021). Predictive modeling for sustainable high-performance concrete from industrial wastes: A comparison and optimization of models using ensemble learners. *Journal of Cleaner Production, 292*, 126032. https://doi.org/10.1016/j.jclepro.2021.126032

Fonseka, I., Mohotti, D., Wijesooriya, K., Lee, C. K., & Mendis, P. (2023). Influence of graphene oxide on abrasion resistance and strength of concrete. *Construction and Building Materials, 404*, 133280. https://doi.org/10.1016/j.conbuildmat.2023.133280

Fonseka, I., Mohotti, D., Wijesooriya, K., Lee, C. K., & Mendis, P. (2024). Influence of graphene oxide properties, superplasticiser type, and dispersion technique on mechanical performance of graphene oxide-added concrete. *Construction and Building Materials, 428*, 136415. https://doi.org/10.1016/j.conbuildmat.2024.136415

Fraser, V. (2000). *Building the New World: Studies in the Modern Architecture of Latin America 1930–1960*. Verso.

Galusnyak, S. C., Petrescu, L., & Cormos, C.-C. (2022). Environmental impact assessment of post-combustion CO2 capture technologies applied to cement production plants. *Journal of Environmental Management, 320*, 115908. https://doi.org/10.1016/j.jenvman.2022.115908

Geim, A. K., & Novoselov, K. S. (2007). The rise of graphene. *Nature Materials, 6*(3), 183–191. https://doi.org/10.1038/nmat1849

Green, A. A., & Hersam, M. C. (2010). Emerging methods for producing monodisperse graphene dispersions. *Journal of Physical Chemistry Letters, 1*(2), 544–549. https://doi.org/10.1021/jz900235f

Griffiths, S., Sovacool, B. K., Furszyfer Del Rio, D. D., Foley, A. M., Bazilian, M. D., Kim, J., & Uratani, J. M. (2023). Decarbonizing the cement and concrete industry: A systematic review of socio-technical systems, technological innovations, and policy options. *Renewable and Sustainable Energy Reviews, 180*, 113291. https://doi.org/10.1016/j.rser.2023.113291

Haddadian, A., Alengaram, U. J., Ayough, P., Mo, K. H., & Alnahhal, A. M. (2023). Inherent characteristics of agro and industrial by-products based lightweight concrete – A comprehensive review. *Construction and Building Materials, 397*, 132298. https://doi.org/10.1016/j.conbuildmat.2023.132298

Hau Hong, D. L., Mohammed, B. S., Al-Fakih, A., Wahab, M. M. A., Liew, M. S., & Amran, Y. H. M. (2020). Deformation properties of rubberized ECC incorporating nano graphene using response surface methodology. *Materials, 13*(12), 2831. https://doi.org/10.3390/ma13122831

Hong, X., Lee, J., & Qian, B. (2022). Mechanical properties and microstructure of high-strength lightweight concrete incorporating graphene oxide. *Nanomaterials, 12*(5), 833. https://doi.org/10.3390/nano12050833

Horszczaruk, E., Mijowska, E., Kalenczuk, R. J., Aleksandrzak, M., & Mijowska, S. (2015). Nanocomposite of cement/graphene oxide—Impact on hydration kinetics and Young's modulus. *Construction and Building Materials, 78*, 234–242. https://doi.org/10.1016/j.conbuildmat.2014.12.009

Ikram, R., Jan, B. M., & Ahmad, W. (2020). An overview of industrial scalable production of graphene oxide and analytical approaches for synthesis and characterization. *Journal of Materials Research and Technology, 9*(5), 11587–11610. https://doi.org/10.1016/j.jmrt.2020.08.050

Indukuri, C. S. R., Nerella, R., & Madduru, S. R. C. (2019). Effect of graphene oxide on microstructure and strengthened properties of fly ash and silica fume based cement composites. *Construction and Building Materials, 229*, 116863. https://doi.org/10.1016/j.conbuildmat.2019.116863

Inel, M., & Ozmen, H. B. (2006). Effects of plastic hinge properties in nonlinear analysis of reinforced concrete buildings. *Engineering Structures, 28*(11), 1494–1502. https://doi.org/10.1016/j.engstruct.2006.01.017

International Energy Agency. (2022). International Energy Agency (IEA) World Energy Outlook 2022. Recuperado de https://www.iea.org/reports/world-energy-outlook-2022

International Monetary Fund. (2023). *Fiscal Monitor: Climate Crossroads Fiscal Policies in a Warming World*. International Monetary Fund.

Iqra, & Zahid, M. (2024). Impact of graphite nano/microplatelets on the mechanical and durability performance of concrete by incorporating mill scale waste. *Journal of Engineering and Applied Science*. https://doi.org/10.1186/s44147-024-00550-3

Krishnamoorthy, K., Veerapandian, M., Yun, K., & Kim, S.-J. (2013). The chemical and structural analysis of graphene oxide with different degrees of oxidation. *Carbon, 53*, 38–49. https://doi.org/10.1016/j.carbon.2012.10.013

Krishnan, A. K., Wong, Y. C., Zhang, Z., & Arulrajah, A. (2024). A transition towards circular economy with the utilisation of recycled fly ash and waste materials in clay, concrete and fly ash bricks: A review. *Journal of Building Engineering, 98*, 111210. https://doi.org/10.1016/j.jobe.2024.111210

Kurda, R., Salih, A., Shakor, P., Saleh, P., Alyousef, R., Ahmed, H., & Aslani, F. (2022). Mix design of concrete: Advanced particle packing model by developing and combining multiple frameworks. *Construction and Building Materials, 320*, 126218. https://doi.org/10.1016/j.conbuildmat.2021.126218

Labaran, Y. H., et al. (2024). Nano-enhanced concrete: unveiling the impact of nano-silica on strength, durability, and cost efficiency. *Discover Civil Engineering*. https://doi.org/10.1007/s44290-024-00120-9

Li, R., Afzali, S. F., & Mahalec, V. (2023). Environmental impacts of optimal designs of community energy systems under different CO2 footprints of electric grids. *Computers & Chemical Engineering, 178*, 108389. https://doi.org/10.1016/j.compchemeng.2023.108389

Lin, L., Peng, H., & Liu, Z. (2019). Synthesis challenges for graphene industry. *Nature Materials, 18*(6), 520–524. https://doi.org/10.1038/s41563-019-0341-4

Lin, Y., & Du, H. (2020). Graphene reinforced cement composites: A review. *Construction and Building Materials, 265*, 120312. https://doi.org/10.1016/j.conbuildmat.2020.120312

Liu, C., Chen, F., Wu, Y., Zheng, Z., Yang, J., Yang, B., Yang, J., Hui, D., & Luo, Y. (2021). Research progress on individual effect of graphene oxide in cement-based materials and its synergistic effect with other nanomaterials. *Nanotechnology Reviews, 10*(1), 1208–1235. https://doi.org/10.1515/ntrev-2021-0080

Loh, K., Bao, Q., Eda, G., et al. (2010). Graphene oxide as a chemically tunable platform for optical applications. *Nature Chemistry, 2*, 1015–1024. https://doi.org/10.1038/nchem.907

Luna-Romera, J. M., Carranza-García, M., Arcos-Vargas, Á., & Riquelme-Santos, J. C. (2024). An empirical analysis of the relationship among price, demand and CO2 emissions in the Spanish electricity market. *Heliyon, 10*(3), e25838. https://doi.org/10.1016/j.heliyon.2024.e25838

Luo, S., Li, X., Lin, W., & Wang, D. (2022). Effects of graphene oxide on resistance to chloride ion penetration of concrete. *Magazine of Concrete Research, 74*(19), 975–988. https://doi.org/10.1680/jmacr.21.00090

Małkowski, P., Ostrowski, Ł., & Brodny, J. (2018). Analysis of Young's modulus for Carboniferous sedimentary rocks and its relationship with uniaxial compressive strength using different methods of modulus determination. *Journal of Sustainable Mining, 17*(3), 145–157. https://doi.org/10.1016/j.jsm.2018.07.002

Meddage, D. P. P., Fonseka, I., Mohotti, D., Wijesooriya, K., & Lee, C. K. (2024). An explainable machine learning approach to predict the compressive strength of graphene oxide-based concrete. *Construction and Building Materials, 449*, 138346. https://doi.org/10.1016/j.conbuildmat.2024.138346

Mergos, P. E., & Kappos, A. J. (2015). Estimating fixed-end rotations of reinforced concrete members at yielding and ultimate. *Structural Concrete, 16*(4), 537–545. https://doi.org/10.1002/suco.201400067

Mohammed, A., Sanjayan, J. G., Duan, W. H., & Nazari, A. (2015). Incorporating graphene oxide in cement composites: A study of transport properties. *Construction and Building Materials, 84*, 341–347. https://doi.org/10.1016/j.conbuildmat.2015.01.083

Monteiro, P. J. M., Miller, S. A., & Horvath, A. (2017). Towards sustainable concrete. *Nature Materials, 16*, 698–699. https://doi.org/10.1038/nmat4930

Murali, M., Alaloul, W. S., Mohammed, B. S., Musarat, M. A., Al Salaheen, M., Al-Sabaeei, A. M., & Isyaka, A. (2022). Utilizing graphene oxide in cementitious composites: A systematic review. *Case Studies in Construction Materials, 17*, e01359. https://doi.org/10.1016/j.cscm.2022.e01359

Nanjundappa, V. S., Ramakrishnappa, T., Kempahanumakkagari, S., Prakash, H. R., & Praveen, B. M. (2023). Efficient strategies to produce graphene and functionalized graphene materials: A review. *Applied Surface Science Advances, 14*, 100386. https://doi.org/10.1016/j.apsadv.2023.100386

Nazarpour, S., & Waite, S. R. (2016). *Graphene technology: From laboratory to fabrication*. Wiley-VCH.

Onaizi, A. M., Huseien, G. F., Lim, A. S., & N. H., Amran, M., & Samadi, M. (2021). Effect of nanomaterials inclusion on sustainability of cement-based concretes: A comprehensive review. *Construction and Building Materials, 306*, 124850. https://doi.org/10.1016/j.conbuildmat.2021.124850

Preethi, G. R., & Chikkanagoudar, R. S. (2019). A study on influence of graphene oxide powder on compressive strength of concrete. *International Research Journal of Engineering and Technology, 6*(10), 23.

Qin, H., Wei, W., & Hu, Y. H. (2017). Synergistic effect of graphene-oxide-doping and microwave-curing on mechanical strength of cement. *Journal of Physics and Chemistry of Solids, 103*, 67–72. https://doi.org/10.1016/j.jpcs.2016.12.009

Qureshi, T. S., & Panesar, D. K. (2020). Nano reinforced cement paste composite with functionalized graphene and pristine graphene nanoplatelets. *Composites Part b: Engineering, 197*, 108063. https://doi.org/10.1016/j.compositesb.2020.108063

Rady, M., Tawfik, A. B., & Alasow, A. A. (2024). Impact of unit prices on the optimal costs of reinforced concrete beams: A comparative study. *Journal of Engineering Research*. https://doi.org/10.1016/j.jer.2024.01.002

Rao, P. T., Prakash, J., Alexander, R., Shinde, M. J., & Dasgupta, K. (2024). Role of graphene oxide infusion in concrete to elevate strength and fire performance in construction concrete. *Diamond and Related Materials, 147*, 111269. https://doi.org/10.1016/j.diamond.2024.111269

Reddy, P. V. R. K., & Prasad, D. R. (2023). The role of graphene oxide in the strength and vibration characteristics of standard and high-grade cement concrete. *Journal of Building Engineering*. https://doi.org/10.1016/j.jobe.2022.105481

Salami, B. A., Mukhtar, F., Ganiyu, S. A., Adekunle, S., & Saleh, T. A. (2023). Graphene-based concrete: Synthesis strategies and reinforcement mechanisms in graphene-based cementitious composites (Part 1).

Construction and Building Materials, 396, 132296. https://doi.org/10.1016/j.conbuildmat.2023.132296
Salehi, M., & Sideris, P. (2020). Enhanced Rayleigh damping model for dynamic analysis of inelastic structures. *Journal of Structural Engineering, 146*(10), 04020216. https://doi.org/10.1061/(ASCE)ST.1943-541X.0002732
Sanalkumar, A., & Yang. (2024). *Advancements in Geopolymer Concrete: A Detailed Review of Recent Progress*. Cham: Springer.
Scott, M. H., & Fenves, G. L. (2006). Seismic evaluation of reinforced concrete frame structures with masonry infills using pushover analysis. *Journal of Structural Engineering, 132*(2), 244–252. https://doi.org/10.1061/(ASCE)0733-9445(2006)132:2(244)
Serrano-Luján, L., Víctor-Román, S., Toledo, C., et al. (2019). Environmental impact of the production of graphene oxide and reduced graphene oxide. *SN Applied Sciences, 1*, 179. https://doi.org/10.1007/s42452-019-0193-1
Shamsaei, E., Basquiroto de Souza, F., Yao, X., Benhelal, E., Akbari, A., & Duan, W. (2018). Graphene-based nanosheets for stronger and more durable concrete: A review. *Construction and Building Materials, 183*, 642–660. https://doi.org/10.1016/j.conbuildmat.2018.06.201
Sun, W., Sun, Y., & Liu, C. (2024). An mass ratio of permanent loads to variable loads of reinforced concrete buildings. *Journal of Asian Architecture and Building Engineering*. https://doi.org/10.1080/13467581.2024.2343802
Tallentire, J. (2022). The new "gold rush": Graphene's research renaissance. In J. Baker & J. Tallentire (Eds.), *Graphene: The route to commercialisation* (pp. 201–220). CRC Press.
Tarpani, R. R. Z., Yunusa-Kaltungo, A., Su, M., Manu, P., Cheung, C. M., Watson, M., Ladislaus, P., & Gallego-Schmid, A. (2024). Environmental assessment of cement production with added graphene. *Cleaner Environmental Systems, 14*, 100206. https://doi.org/10.1016/j.cesys.2024.100206
Tayebani, B., Said, A., & Memari, A. (2023). Less carbon producing sustainable concrete from environmental and performance perspectives: A review. *Construction and Building Materials, 404*, 133234. https://doi.org/10.1016/j.conbuildmat.2023.133234
Udumulla, D., Ginigaddara, T., Jayasinghe, T., Mendis, P., & Baduge, S. (2024). Effect of graphene oxide nanomaterials on the durability of concrete: A review on mechanisms, provisions, challenges, and future prospects. *Materials*. https://doi.org/10.3390/ma17102411
UNAM Seismology Group. (2015). Papanoa, Mexico earthquake of 18 April 2014 (M w 73). *Geofísica Internacional, 363*, 386.
Vandanapu, S. N., & Krishnamurthy, M. (2018). Seismic performance of lightweight concrete structures. *Advances in Civil Engineering, 2018*, 1–6.
Walunjkar, P. M., & Bajad, M. N. (2023). Review on effect of graphene oxide reinforcement on properties of cement concrete. *Mater Today Proceedings*. https://doi.org/10.1016/j.matpr.2023.09.085
Wang, L., Zhang, S., Zheng, D., Yang, H., Cui, H., Tang, W., & Li, D. (2017). Effect of graphene oxide (GO) on the morphology and microstructure of cement hydration products. *Nanomaterials, 7*(12), 429. https://doi.org/10.3390/nano7120429
Wang, W., Zhong, Z., Kang, X., & Ma, X. (2023). Physico-mechanical properties and micromorphological characteristics of graphene oxide reinforced geopolymer foam concrete. *Journal of Building Engineering, 72*, 106732. https://doi.org/10.1016/j.jobe.2023.106732
Warner, J. H., Francesca, S., Mark, H., & Graham, F. (2013a). "Graphene in Industry, Commercialization Challenges, and Economics. In H. Jamie (Ed.), *En Graphene: An Introduction to the Fundamentals and Industrial Applications* (pp. 243–267). Wiley.
Warner, J. H., Schaffel, F., Heeney, M., & Spencer, G. F., et al. (2013b). Graphene in industry, commercialization challenges, and economics. In J. H. Warner (Ed.), *Graphene: An introduction to the fundamentals and industrial applications* (pp. 243–267). Wiley.
Xue, J., & Shinozuka, M. (2013). Rubberized concrete: A green structural material with enhanced energy-dissipation capability. *Construction and Building Materials, 42*, 196–204. https://doi.org/10.1016/j.conbuildmat.2013.01.005
Yang, H., Cui, H., Tang, W., Li, Z., Han, N., & Xing, F. (2017). A critical review on research progress of graphene/cement based composites. *Composites Part a: Applied Science and Manufacturing, 102*, 273–296. https://doi.org/10.1016/J.COMPOSITESA.2017.07.019
Yeke, L., & Yu, Z. (2021). Effect of graphene oxide on mechanical properties of UHPC and analysis of micro-control mechanism. *Materials Research Express, 8*, 095001. https://doi.org/10.1088/2053-1591/ac2015
Zareef MAME. (2010). Conceptual and structural design of buildings made of lightweight and infra-lightweight concrete.
Zeng, H., Qu, S., Tian, Y., Hu, Y., & Li, Y. (2022). A review of graphene oxide/cement composites: Performance, functionality, mechanisms, and prospects. *Journal of Building Engineering, 53*, 104502. https://doi.org/10.1016/j.jobe.2022.104502
Zeng, H., Qu, S., Tian, Y., Hu, Y., & Li, Y. (2023). Recent progress on graphene oxide for next-generation concrete: Characterizations, applications and challenges. *Journal of Building Engineering, 69*, 106192. https://doi.org/10.1016/j.jobe.2023.106192
Zhang, X., Wu, Z., Xie, J., Hu, X., & Shi, C. (2024). Trends toward lower-carbon ultra-high performance concrete (UHPC) – A review. *Construction and Building Materials, 420*, 135602. https://doi.org/10.1016/j.conbuildmat.2024.135602

Publisher's Note

D. Domínguez-Santos Ph.D. in Civil Engineering. Associated professor at Universidad de Talca (Chile). Full-time research scientist, tenured

P. Muñoz Ph.D. in Industrial Engineering. Full professor at Universidad Internacional de La Rioja (Spain), visiting professor at Universidad Autonoma de Chile (Chile). Full-time research scientist, tenured

J. O. Morales-Ferreiro Ph.D. in Mechanical Engineering. Associated professor at Universidad Mayor (Chile). Full-time research scientist, tenured

C. Acuña Ph.D. in Physics. Associated professor at Pontificia Universidad Católica de Chile (Chile). Full-time research scientist, tenured

D. E. Diaz-Droguett MSc. in Materials. Lecturer professor at Pontificia Universidad Católica de Chile (Chile). Part-time research scientist, non-tenured

Elvira Villaro Ph.D. in Chemistry. Chief technology officer at Avanzare (Spain). Full-time